JGR Planets

RESEARCH ARTICLE

10.1029/2025JE009303

Key Points:

- Joint inversion of seismic, geodetic, and electrical conductivity data reduces the non-uniqueness in Mars interior and thermal evolution
- Two solution families emerge for homogeneous mantles, with electrical conductivity data favoring low Mg content, high-temperature models
- Output layered mantle models highlight the need for tighter constraints on conductivity profile slope and lithospheric thickness

Supporting Information:

Supporting Information may be found in the online version of this article.

Correspondence to:

M. Drilleau,
drilleau@ipgp.fr

Citation:

Drilleau, M., Samuel, H., Verhoeven, O., Rivoldini, A., Collinet, M., Garcia, R. F., & Lognonné, P. (2026). Constraining the thermochemical structure of Mars through joint inversion of multidisciplinary geophysical data. *Journal of Geophysical Research: Planets*, *131*, e2025JE009303. https://doi.org/10.1029/2025JE009303

Received 23 JUL 2025
Accepted 23 DEC 2025

Constraining the Thermochemical Structure of Mars Through Joint Inversion of Multidisciplinary Geophysical Data

Mélanie Drilleau[1], Henri Samuel[1], Olivier Verhoeven[2], Attilio Rivoldini[3], Max Collinet[4], Raphaël F. Garcia[5], and Philippe Lognonné[1]

[1]Université Paris Cité, Institut de physique du globe de Paris, CNRS, Paris, France, [2]Laboratoire de Planétologie et Géosciences, Nantes Université, Université d'Angers, Le Mans Université, CNRS, UMR 6112, UAR 3281, Observatoire des Sciences de l'Univers de Nantes Atlantique, Nantes, France, [3]Royal Observatory of Belgium, Brussels, Belgium, [4]Institute of Life, Earth and Environment (ILEE), Namur University, Namur, Belgium, [5]Institut Supérieur de l'Aéronautique et de l'Espace ISAE-SUPAERO, Université de Toulouse, Toulouse, France

Abstract Understanding Mars' deep interior is essential to reconstruct its geological history, thermal evolution, and present-day dynamics. To this end, the NASA InSight mission has provided unprecedented seismic observations. However, strong trade-offs between temperature and composition in seismic interpretations continue to limit our ability to resolve interior models. To address this challenge, we account for electromagnetic induction data from Mars Global Surveyor as an additional, independent constraint. We develop a joint probabilistic inversion framework that simultaneously fits seismic body wave arrival times, electrical conductivity, the k_2 Love number, and the moment of inertia. A key feature of our approach is the integration of Mars' long-term thermal evolution within the forward model, along with mineral physics and petrology data, to better constrain geodynamical parameters. We explore three different mantle compositions (Sanloup et al., 1999, https://doi.org/10.1016/s0031-9201(98)00175-7; Taylor, 2013, https://doi.org/10.1016/j.chemer.2013.09.006; Yoshizaki & McDonough, 2020, https://doi.org/10.1016/j.gca.2020.01.011) and consider both radially homogeneous and heterogeneous (with a basal molten layer (Samuel et al., 2023, https://doi.org/10.1038/s41586-023-06601-8)) mantle scenarios. For homogeneous mantle models, two families of solutions emerge regardless of the bulk composition: one with low Mg content and high potential temperature, which better reproduces electrical conductivity data due to a thicker lithosphere, and another with high Mg content and lower potential temperature. Models with a heterogeneous mantle reproduce electrical conductivity data less accurately, due to thinner lithospheres, and the mantle composition of Yoshizaki and McDonough (2020, https://doi.org/10.1016/j.gca.2020.01.011) appears to be less consistent with the full data set. To further refine models of Mars' interior, future efforts should focus on acquiring electromagnetic data with reduced uncertainties and seismically constraining more precisely the depth of mantle discontinuities associated with mineral phase transitions.

Plain Language Summary Understanding the deep interior of Mars is essential for reconstructing the planet's formation, geological evolution, and present-day internal dynamics. NASA's InSight mission has provided valuable seismic data, but interpreting this information remains challenging because variations in temperature and composition can produce similar seismic signals. To address this limitation, we combine seismic observations with electrical conductivity data collected by the Mars Global Surveyor spacecraft. We develop a new probabilistic modeling approach that jointly incorporates several data sets: seismic arrival times, electrical conductivity, the k_2 Love number, and the planet's moment of inertia. Our method also integrates Mars' long-term thermal evolution along with mineral physics and petrology constraints to better characterize its internal structure. We examine different mantle compositions and compare models with a homogeneous mantle with those with a molten layer at the base of the mantle. Homogeneous models tend to produce two solutions: one with a hotter interior and lower magnesium content that fits electrical data well, and the other with cooler temperatures and higher magnesium content. Models with a basal layer generally show poorer agreement with the electrical conductivity data. Improved electromagnetic measurements and tighter seismic constraints are key to advancing our understanding of Mars' interior.

1. Introduction

The present-day radial structure of terrestrial planets is the result of their long-term evolution and provides a crucial anchorage on their dynamical and thermal history. For this reason, inferring the thermochemical structure of the planets from geophysical observables is a fundamental goal of space exploration. Space missions have gradually collected different types of geophysical data, each of these providing further information about the interior structure of our neighboring planets, and especially the planet Mars. The NASA InSight (Interior Exploration Using Seismic Investigations, Geodesy, and Heat Transport) mission (Banerdt et al., 2020) which operated for 1,440 Martian days, marked a turning point in the exploration of Mars. Thanks to its seismometer (Lognonne et al., 2019), the mission has significantly improved our knowledge about the interior structure of Mars. In particular, the determination of the size of the core from the detection of S waves reflected at a solid-liquid interface located at the bottom of the solid mantle (Stähler et al., 2021) is notably more precise than previous estimates obtained from geodesy data (e.g., Yoder et al., 2003). Using a larger data set with seismic waves propagating through the core, Irving et al. (2023) found a smaller and denser core compared to the previous estimate in Stähler et al. (2021). By measuring the nutations of Mars with the Rotation and Interior Structure Experiment (RISE) on InSight, Le Maistre et al. (2023) independently confirmed the core radius deduced from seismic observations. Recently, Samuel et al. (2023) demonstrated that measurements of anomalously slow propagating P-waves diffracted along the core-mantle boundary are compatible with a molten silicate layer above the liquid metallic core. Additionally, the observation of direct and surface-reflected body wave phases has allowed the thermal structure of the Martian mantle to be refined (Drilleau et al., 2022; Durán et al., 2022; Khan et al., 2021). Using receiver functions, Knapmeyer-Endrun et al. (2021) revealed the layered structure of the Martian crust, with either two or three crustal layers.

Despite these improvements in our understanding of the interior structure of Mars, most studies based on the inversion of geophysical data focus on a specific type of observation. They either consider separately electromagnetic data (e.g., Civet & Tarits, 2014), gravity and topography data (e.g., Wieczorek & Zuber, 2004), the degree-two tidal Love number k_2 and the moment of inertia (e.g., Khan & Connolly, 2008), seismological data (e.g., Drilleau et al., 2022), or the measured nutation of the rotation axis (Le Maistre et al., 2023). However, using different types of data, each with varying sensitivities to the planet's structure in terms of depth, composition, and temperature, makes it challenging to directly compare interior structure models derived from separate studies. In the recent literature, the most commonly used data in joint inversion studies are seismic and geodetic data (k_2 and moment of inertia) (e.g., Irving et al., 2023; Samuel et al., 2023; Stähler et al., 2021). A first attempt to jointly invert for seismological, geodetic, and gravity and topography data to infer the global structure of Mars has been performed in Drilleau et al. (2024). They showed that compared to a 1D structure, models with lateral variations of crustal thickness show two possible interpretations of the thermal evolution of Mars, with either a hot or cold scenario at the present-day. The effect on the inference using other independent data set is often tested in a second step. For example, in Samuel et al. (2023), after inferring the 1D structure of Mars from seismic and geodetic data, the size of a subset of the best-fitting models has been reduced by comparing the predicted nutation of those models with observations done by RISE (Le Maistre et al., 2023). In the context of Mars, a multi-observable inversion approach, providing a robust unified thermochemical model of Mars from the crust to the core, largely remains an understudied field. One solution for determining structure models that agree with different types of data and to obtain consistent and robust estimates of the parameters, is to simultaneously invert for all the considered geophysical observables, using an internally consistent approach in which the observables and model parameters are related through a unique model (e.g., Afonso et al., 2013).

A difficulty encountered in the inversion of seismic data is the trade-off between the effects of temperature and composition (e.g., Afonso et al., 2013). Several Martian bulk compositions have been tested in for example, Stähler et al. (2021), Durán et al. (2022), and Irving et al. (2023), yet the inversion results consistently yield similar misfits regardless of the assumed mantle composition. Because the electrical conductivity of mantle minerals is more sensitive to temperature and iron content than are densities and acoustic velocities, complementing seismic and geodetic data with electrical conductivity data represents a new step toward refining inferences about the interior structure of Mars (e.g., Mocquet & Menvielle, 2000, 2009; Verhoeven & Vacher, 2016; Verhoeven et al., 2005). Despite many progresses made in the last decade in imaging the electrical structure of the Earth by studying different sources of the electromagnetic field (see e.g., Grayver, 2024 for a recent review), very few studies have been reported for Mars. Compared to Earth, Mars' electromagnetic environment is not well known, which makes it difficult to separate inducing and induced components of the magnetic field. To our knowledge, electromagnetic sounding on Mars has received little attention so far, with the exception of the study by Civet and Tarits (2014), who derived a radial conductivity profile of the Martian mantle from Mars Global Surveyor (MGS) magnetometer data. From Martian mantle convection models and assuming the bulk silicate Mars composition of Wänke et al. (1994), Ruedas and Breuer (2021) derived synthetic electrical conductivity, seismic velocity, and density distributions. These models were found to be in good agreement with the 1D electrical conductivity profile in Civet and Tarits (2014) between ∼300 and ∼1000 km depth. The first attempts to retrieve data recorded by the InSight fluxgate magnetometer (IFG) for electromagnetic sounding were unsuccessful due to contamination from spacecraft-generated signals and limited data coverage (Mittleholz et al., 2020). Grimm et al. (2024) have also highlighted the additional difficulty in dealing with the existence of possible lateral heterogeneities. More recently, progress has been made in Mittleholz et al. (2025), which derived the local C-response from the InSight data and found that regardless of the inducing field geometry, a relatively high crustal conductivity is required (larger than 10^{-2} S/m). Because of the relatively short time period during which the IFG continuously collected the data, the maximum depth of sounding remains limited to the crust.

Over the past few decades, the reliability of high-pressure and high-temperature measurements of mineral physics properties, such as elasticity and electrical conductivity of mantle minerals, has improved significantly. This improvement now presents a new opportunity to impose additional independent constraints on Mars' interior through the joint inversion of different geophysical data sets. In this study, we present a synergetic strategy in which we simultaneously invert seismic, geodetic, and electrical conductivity data to constrain interior models of Mars, using a probabilistic approach. By investigating the extent to which interior structure models constrained by seismic and geodetic measurements (e.g., Irving et al., 2023; Samuel et al., 2023) can be further refined by incorporating electrical conductivity data, our objective is to assess whether temperature and compositional effects can be effectively decoupled.

The paper is organized as follows: Section 2 presents the data we considered, Section 3 summarizes the inversion methodologies (model parameterization, forward and inverse problems), Section 4 presents the inversion results, Section 5 discuss the inversion results, and Section 6 summarizes the main findings of this study.

2. Geophysical Data

In this study, we call 'data' the following geophysical quantities: the normalized moment of inertia factor (MoI), the k_2 Love number, the body wave arrival times, and the electrical conductivity as a function of depth between 400 and 900 km.

The geodetic data we consider are the values of the normalized MoI factor and k_2 Love number of Konopliv et al. (2020) ($\mathrm{MoI} = 0.3634 \pm 0.00006$ and $k_2 = 0.174 \pm 0.008$).

We use the body wave arrival time database of Drilleau et al. (2024) (Table S1.1 in Supporting Information S1) which contains 31 seismic events. In addition to the direct P- and S-phases, this database includes phases reflecting below the surface (PP, PPP, SS, SSS) and at the core-mantle boundary (ScS), depth phases (pP, sP, sS), and two core-transiting seismic phase (SKS) initially identified by Irving et al. (2023). We also consider the P-diffracted wave reflected at the core-mantle boundary (CMB), first observed by Horleston et al. (2022) and interpreted either as a Pdiff in models without a basal molten mantle layer, or as a PbdiffPcP when such a layer is present (Samuel et al., 2023). Among the 31 seismic events, two result from meteoroid impacts (S1000a and S1094b). Due to the unknown origin time of the seismic events, we rely on differential times measured relative to the phase arrivals of the P- and S-waves.

We also consider the electrical conductivity profile derived by Civet and Tarits (2014) from Mars Global Surveyor (MGS) magnetometer data. The magnetometer time series were used to compute the induced response of the mantle at different frequencies, which allows to sound the mantle at different depths and deduce the electrical conductivity of the mantle down to 1,300 km depth. In order to avoid affecting our inferences by possible heterogeneities in the upper part of the mantle resulting from the crustal dichotomy and the lack of resolution in its lower part of the mantle, we focus on the region where this profile shows the smaller uncertainties, that is, between 400 and 900 km depth. The electrical conductivity profile of Civet and Tarits (2014) is made of 9 layers of 180 km (see their Figure 4). To get rid of this layered parameterization, we use a continuous version of this model by assigning the electrical conductivity value of each layer to the middle of the layer and connecting these points with line segments.

3. Inversion Methodology

3.1. Model Parameterization

3.1.1. Bulk Silicate Models

Determining the Mg number (Mg# = Mg/(Mg + Fe)) and the abundance of Heat-Producing Elements (HPE) in the Martian mantle is essential for constraining its compositional, thermal, and geodynamical evolution. For this reason, we improved the models of Samuel et al. (2023) and Drilleau et al. (2024) considering the Mg# as a parameter of the inversion, instead of leaving it fixed, and the Heat-Producing Elements (HPE) content varies accordingly as explained below.

The different models of bulk silicate Mars are recreated from chondritic compositions (Wasson & Kallemeyn, 1988) using the constraints specified in Sanloup et al. (1999), Taylor (2013), and Yoshizaki and McDonough (2020) (hereafter named EH45, TA, and YM, respectively) but keeping the FeO concentration (and therefore the Mg#) as a free parameter. This choice is justified by the fact that the Mg# of the Martian mantle that is necessary to account for the formation of Martian meteorites and basalts analyzed in situ appears to be highly variable (Collinet et al., 2015; Taylor, 2013). In addition, the bulk Fe/Si and FeO/(Fe + FeO) of chondrites are highly variable, including between groups characterized by similar oxygen isotopes and nucleosynthetic anomalies. The average FeO content of the mantle has thus proven challenging to estimate from geochemical and petrological models alone.

The TA model is obtained by taking 100% of the CI composition (Wasson & Kallemeyn, 1988) and correcting the concentrations of moderately volatile elements (MVE) by multiplying them by the ratios of MVEs to refractory elements presenting similar partition coefficients in igneous systems (see Table 5 in Taylor (2013)). The EH45 model is obtained by mixing 45%–55% of the EH and H chondritic compositions. Finally, the YM model is calculated from the CI composition by increasing the concentration of refractory elements (RE; Ca, Al, Ti, U, Th, etc.) until attaining a CI-normalized abundance of 2.26, as suggested for the source of shergottites (Yoshizaki & McDonough, 2020), and then by applying the same MVE corrections as for the Taylor (2013) model. The FeO content of all these models is then varied by keeping the chondritic Mg concentration constant but progressively removing Fe to match a series of Mg#. Given that Mars' Mg# remains poorly constrained (Collinet et al., 2023), we selected a range of Mg# values from 0.66 to 0.86. The latter end-member represents the minimum Mg# of the mantle needed to produce depleted shergottites. The compositions with Mg#s nearly identical to the different bulk silicate models (i.e., 0.73 for EH45, 0.75 for TA and 0.79 for YM) are found to be nearly identical to the corresponding published compositions. This method thus allows us to isolate the effect of the Mg# on the mantle mineralogy from the other compositional variables (e.g., Mg/Si, RE/Mg, RE/MVE) that have been proposed by available geochemical models (Sanloup et al., 1999; Taylor, 2013; Yoshizaki & McDonough, 2020).

3.1.2. Geodynamical Parameters

Following Samuel et al. (2023) and Drilleau et al. (2021, 2022), the inversion approach incorporates a geodynamic forward modeling step that assumes a spherically symmetric planet composed of a liquid metallic core and a silicate mantle convecting under an evolving lithosphere, which includes a crust enriched in heat-producing elements (HPEs). In a set of models we further consider the presence of a stable stratified silicate layer above the metallic core. This basal mantle layer (BML) is enriched in iron and HPE relative to the overlying mantle (Samuel et al., 2023), as suggested by seismic observations (Durán et al., 2022; Horleston et al., 2022; Posiolova et al., 2022). The thermochemical evolution of the planet is then computed for 4.5 Gyr, and depends on the values of governing parameters that are inverted for. These consist in quantities that define the initial thermal state of the planet, the partitioning of HPEs between the core and the mantle, the core size, and the thickness of the BML when present, the mantle rheology and thermal conductivity that determine the efficiency of heat transfer across planetary envelopes, or the Mg content in the silicate envelope. This geodynamic modeling involves mantle solidus and liquidus: crustal formation results from shallow melt extraction, and seismic velocities are affected by the presence of melt (Samuel et al., 2019, 2023). Following Samuel et al. (2021), mantle melting curves are those proposed in Duncan et al. (2018), which are modified by the presence of iron (Elkins-Tanton, 2008): larger iron content shifts melting temperatures toward lower values. Therefore, mantle melting curves for each model depend on the value of the Mg# associated with the model. The list of inverted parameters and the corresponding prior bounds considered are summarized in Table 1. Note that we considered a wider range for thermal conductivity k_d in the enriched basal

Table 1

List of Inverted Parameters, and the Corresponding Prior Bounds Considered

Inverted parameter	Meaning	Range	Units
E^*	Mantle effective activation energy	100–500	kJ/mol
V^*	Mantle effective activation volume	0–10	$\mathrm{cm^3/mol}$
η_0	Mantle reference viscosity	10^{20}–10^{23}	Pa s
T_{m_0}	Initial uppermost mantle temperature	1,700–2,000	K
T_{c_0}	Initial CMB temperature	$T_{c_0} - T_{m_0} = 300$–600	
R_c	Core radius	1,400–2,000	km
K_S	Core isentropic bulk modulus at CMB	120–200	GPa
K_S'	Pressure derivative of K_S	2–7	–
k_d	BML thermal conductivity	1–20	$\mathrm{W\ m^{-1}\ K^{-1}}$
D_d	BML thickness	100–600	km
Mg#	Mg number	0.66–0.86	–
V_{S_1}	V_S in the upper crust (layer 1)	1.0–3.0	km/s
V_{S_2}	V_S in the mid-crust (layer 2)	2.0–3.5	km/s
V_{S_3}	V_S in the lower crust (layer 3)	3.9–4.4	km/s
V_P/V_S	V_P/V_S in the entire crust	1.7–1.9	–
Δ	Source epicentral distance	0–180 (except for S1000a and S1094b)	°
p_{Depth}	Source depth	5–200 (except for S1000a and S1094b)	km

Note. The subscripts "0" indicate initial values for quantities that vary in time. k_d and D_d are only inverted when a BML is considered.

mantle layer compared to Samuel et al. (2023). These low values account for the effect of iron and the presence of melt that both decrease the value of thermal conductivity (Guerrero et al., 2023; Hsieh et al., 2018, 2024).

Seismic velocities and the density in the mantle are computed from the present-day thermal profile with `Perple_X` (Connolly, 2005) using the thermodynamic database of Stixrude and Lithgow-Bertelloni (2021). For comparison with previous studies (e.g., Drilleau et al., 2024; Durán et al., 2022; Irving et al., 2023; Khan et al., 2021; Samuel et al., 2023) and to assess the effect of using a different thermodynamic database, we also provide inversion results obtained with the database Stixrude and Lithgow-Bertelloni (2011) in Section 5.1.

Although crustal thickness is an output of the geodynamical modeling, the seismic velocities and the structure of the crust are directly inferred from the geophysical data. This is because the crust's mineralogy and internal structure are poorly constrained and likely not in thermodynamic equilibrium, which prevents the use of static thermodynamic models. Therefore, following for example, Drilleau et al. (2022, 2024), Samuel et al. (2023), and based on constraints from receiver function analyses (Knapmeyer-Endrun et al., 2021), we model the crust using three layers of variable thickness and seismic velocities. For the core, we assume it is well mixed and convecting, as in Irving et al. (2018, 2023) and Samuel et al. (2023), and calculate its elastic properties using a third-order isentropic Birch–Murnaghan equation of state. This approach does not require prior assumptions about the core composition, and the equation of state implicitly provides a thermodynamically consistent relationship between density and acoustic wave velocity if the core is isentropic.

3.1.3. Electrical Conductivity From Earth-Based Laboratory Measurements

Thanks to laboratory measurements of the electrical conductivity of minerals at high temperature and pressure, an estimation of the electrical conductivity of the Martian mantle can be obtained. Electrical conductivity is a function of mineral composition, temperature, pressure, water and iron content, and oxygen fugacity (see e.g., Fullea, 2017; Khan, 2016; Naif et al., 2021; Ruedas & Breuer, 2021; Yoshino, 2010 for reviews).

At Earth conditions, the electrical conductivity is modeled as the sum of three different conduction mechanisms: ionic, small polaron, and proton conduction. At Martian conditions, small polaron conduction dominates the other

Table 2
Values of Model Parameters for Minerals and Mineral Phases Small Polaron Conductivity

Mineral	$\log \sigma^h_{0,ref}$ (S/m)	ΔE^h_{ref} (eV)	a	α^h	ΔV(cm^3/mol)	Reference
Olivine	2.69	2.07	2.56	0.96	–	Wang et al. (2014)
Orthopyroxene	3.67	2.67	−1.11	1.88	–	Wang et al. (2014)
Clinopyroxene	3.20	2.74	−1.11	1.88	–	Wang et al. (2014)
Garnet	3.35	2.52	0	1.91	–	Verhoeven and Vacher (2016)
Wadsleyite	3.29	1.67	0	0.83	–	Verhoeven and Vacher (2016)
Ringwoodite	2.92	2.31	0	2.49	–	Verhoeven and Vacher (2016)
Ferropericlase	2.69	1.56	0	1.49	−0.26	Verhoeven and Vacher (2016)
Al-bearing bridgmanite	1.87	1.30	0	1.28	−0.26	Verhoeven and Vacher (2016)
Ilmenite	1.18	0.82	0	0	−1.50	Katsura et al. (2007)
Stishovite	1.57	1.12	0	0	–	Yoshino et al. (2014), Al-free 178 ppm water sample
Feldspar	4.12	1.67	0	0	–	Yang et al. (2012), dry sample
Kyanite	3.35	2.52	0	1.91	–	Verhoeven and Vacher (2016), same as garnet as closest mineral phase

Note. Activation volume for ferropericlase and Al-bearing bridgmanite are from the review of Vacher and Verhoeven (2007).

two conduction mechanisms, because of the very high iron content of the mantle (Verhoeven & Vacher, 2016). We therefore calculate the electrical conductivity of the Martian mantle from this conduction mechanism only. Generalizing the modified Arrhenius law introduced by Wang et al. (2014) and Verhoeven and Vacher (2016) modeled the electrical conductivity σ of 9 mantle minerals or phases (olivine, wadsleyite, ringwoodite, orthopyroxene, clinopyroxene, garnet, Al-free bridgmanite, Al-bearing bridgmanite, and ferropericlase) as a function of temperature T, pressure P and iron content X_{Fe} as:

$$\sigma\left(T,P,X_{Fe}\right) = \sigma^h_{0,\mathrm{ref}}\left(\frac{X_{Fe}}{X_{\mathrm{ref}}}\right)^a e^{-\left(\frac{\Delta E^h_{\mathrm{ref}}-\alpha^h X_{Fe}^{1/3}+P\Delta V}{k\,T}\right)}, \tag{1}$$

where a gives the iron content power-law dependence of σ^h_0 and α^h is a constant accounting for geometrical factors. $\sigma^h_{0,\mathrm{ref}}$ is the limiting value of σ when the temperature goes to infinity and when $X_{Fe} = X_{\mathrm{ref}}$, and $\Delta E^h_{\mathrm{ref}}$ is the activation energy observed at very low iron concentrations and $P = 0$. The iron fraction reference X_{ref} was set to 0.1 to ground the Arrhenius law on terrestrial values (Xu et al., 2000). The values of the parameters $\sigma^h_{0,\mathrm{ref}}$, $\Delta E^h_{\mathrm{ref}}$, a and α^h are different from each mineral phase and were calculated to fit the various conductivity measurements of iron bearing minerals at reference conditions. Those values can be found in Table 2.

To account for the variety of mineral phases that are predicted from Gibbs energy minimization of Martian bulk compositions, we also provide parameter values for ilmenite, stishovite, feldspar and kyanite in Table 2. For these minor mineral phases, a and α^h are set to 0, as either they are devoid of iron or the effect of iron is not known. To calculate the rock conductivity from individual mineral phases we use the effective medium averaging scheme, which appears to be one of the best methods to model the electrical conductivity of the Earth's mantle (Han & Clark, 2021).

3.2. Forward Problem

This section summarizes the different steps of the forward problem used to compute synthetic geodetic, seismic, and electrical conductivity data, from model parameter values. The procedure largely follows that described in Samuel et al. (2023) and Drilleau et al. (2024), with several key improvements: (a) the Mg# is now a model parameter rather than assumed fixed; (b) the solidus is Mg# dependent; (c) the HPE content varies according to Mg#; and (d) electrical conductivity data are incorporated into the inversion framework.

The computation of an interior structure from the model parameters is done in six main steps: (a) Assuming one of the three bulk silicate mantle compositions (EH45, TA, or YM), and assuming the presence or absence of a BML, geodynamical parameters and location of marsquakes are sampled from the prior distribution (Table 1). (b) As explained in Section 3.1.2, the present-day thermo-chemical state of the planet is used to calculate the density, as well as the radial P- and S-wave seismic velocity profiles of Mars. (c) If the normalized MoI factor cannot satisfy the value of Konopliv et al. (2020) within four sigmas, the model is rejected. (d) If the crustal thickness of the model falls outside the 30–72 km range determined by Wieczorek et al. (2022), which is derived from gravity and topography data and anchored by the crustal thickness beneath the InSight lander, the model is rejected. If the model is retained, (e) the simulated data sets are computed. The k_2 Love number is calculated following Alterman et al. (1959), Takeuchi and Saito (1972), and the differential body wave arrival times are computed using the `TauP` toolkit (Crotwell et al., 1999) based on randomly sampled marsquake locations. The electrical conductivity profile is determined as explained in Section 3.1.3. (f) The final step involves determining the cost function, before the acceptance/rejection stage.

3.3. Inverse Problem

The inverse problem considered here is highly nonlinear and is addressed using a Bayesian approach (e.g., Tarantola, 2005). Specifically, a Markov chain Monte Carlo (McMC) algorithm is used to sample solutions that not only fit the observational data within their uncertainties, but also adhere to the prior constraints detailed in Table 1.

We denote the model parameters and the observed data by the vectors **p** and **d**, respectively. These quantities are linked through the forward operator A, such that $\mathbf{d} = A(\mathbf{p})$. The operator A, which is both non-linear and non-analytic, encapsulates the forward problem outlined in Section 3.2. The parameters **p** are listed in Table 1 and the data **d** are described in Section 2. In this context, the inverse problem is addressed probabilistically through the posterior distribution $P(\mathbf{p}|\mathbf{d})$, which quantifies the likelihood that the model parameters **p** assume a given configuration, conditional on the observed data **d**. This posterior distribution is informed by the prior distribution $P(\mathbf{p})$, which encapsulates our prior knowledge or assumptions about the parameters (Table 1). The relationship between the prior and the posterior PDF (Probability Density Function) is governed by Bayes' theorem:

$$P(\mathbf{p}|\mathbf{d}) = \frac{P(\mathbf{d}|\mathbf{p})P(\mathbf{p})}{\sum_{\mathbf{p}\in\mathcal{M}} P(\mathbf{d}|\mathbf{p})P(\mathbf{p})}, \tag{2}$$

where $\mathcal{M}$ denotes the set of all possible configurations within the parameter space. The posterior distribution $P(\mathbf{p}|\mathbf{d})$ is conditioned by the cost function $\mathcal{S}$, which serves as a metric to assess the agreement between model predictions and observational data.

Assuming that the data noise follows a Laplacian distribution (L_1 norm), and that observational uncertainties and computational errors among the data sets considered are independent, the cost function is therefore evaluated as follows:

$$\mathcal{S} = \frac{|k_2^{obs} - k_2^{cal}|}{\Delta_{k_2}} + \sum_{i}^{N_t} \frac{|t_i^{obs} - t_i^{cal}|}{\Delta_{t_i}} + \sum_{i}^{N_\sigma} \frac{|\log(\sigma_i^{obs}) - \log(\sigma_i^{cal})|}{\Delta \log(\sigma_i)}, \tag{3}$$

where the superscripts refer to observed data (obs) and computed data (cal), respectively. k_2, t, and σ are the k_2 Love number, the body wave differential arrival times, and the electrical conductivity data, respectively, and Δ_{k_2}, Δ_t, and Δ_σ denote the uncertainties of either of these. Note that in this study, we consider Δ_{k_2} as the 95% confidence interval reported by Konopliv et al. (2020), that is, 0.016. $N_t = 161$ is the total number of observed differential arrival times from Drilleau et al. (2024). $N_\sigma = 100$ is the total number of electrical conductivity data, regularly sampled as a function of depth between 400 and 900 km, extracted from the smoothed version of the Civet and Tarits (2014)'s profile (see Section 2). t_i^{obs} and σ_i^{obs} therefore indicate the i-th differential time and electrical conductivity data, respectively.

The Metropolis algorithm (Metropolis et al., 1953) is used to infer the posterior distribution of the parameters (Equation 2). The algorithm performs a stochastic exploration of the model space, prioritizing models that provide a good fit to the observed data and remain consistent with prior constraints. Specifically, the Metropolis algorithm samples the model space with a probability density proportional to the target posterior distribution, thereby minimizing the oversampling of low-probability regions.

4. Inversion Results

Two sets of inversions are considered: one assuming a compositionally homogeneous mantle (non-BML), and another incorporating a basal mantle layer (BML) above the core. For each set, three distinct mantle compositional models (EH45, TA, and YM) are tested against the observed data.

4.1. Contribution of Each Type of Data

To investigate the influence of each data set on the inferred model parameters, we first performed separated inversions of the three geophysical data sets. Figures 1 and 2 show the joint posterior PDFs of the potential temperature (T_p) and Mg#, for inversions of the three separated geophysical data sets (rows) and for the three mantle compositions (columns), considering non-BML and BML models, respectively. The result of the joint inversion is displayed in the fourth row.

A first striking observation is that, regardless of the presence of a BML, models with Mg# < 0.72 are rejected because they lie more than four sigmas away from the observed normalized MoI factor. For non-BML models, inferences obtained using k_2 and body wave arrival times result in a bimodal distribution of T_p, with a "cold" and a "hot" mode, located left and right to ~1600 K. The bimodal distribution arises from a particular interplay of the geodynamical parameters: mantle rheology, the degree of crustal enrichment relative to the primitive mantle, and the initial thermal state. Specific combinations of these parameters promote extensive melting in the shallow mantle during the early evolution of the planet, leading to the formation of a crust thicker than the upper limit of our prior range (>72 km) or to nonphysical depletion in HPE of the shallow mantle upon melting and crustal extraction. For a more detailed discussion see Drilleau et al. (2024) (Section S2.3 in Supporting Information S1). Due to their larger HPE content, YM models have more difficulty producing models with both a large T_p value and a crustal thickness thinner than 72 km. This bimodality in the T_p-Mg# PDFs is also observed to a lesser degree in the BML set (Figure 2) when inverting body wave arrival times.

For all mantle compositions with or without a BML, interior models inferred from the mantle electrical conductivity data evidently yield larger T_p. The results clearly illustrate the trade-off between T_p and Mg#, which unsurprisingly results from the fact that the electrical conductivity data can be reproduced equally well with a hot temperature profile and a low iron content, and vice versa. Among the "hot" models, a bimodal distribution is found in the T_p-Mg# PDFs for the non-BML setting (Figures 1c1 and 1c2), which is different from the one observed in the inversions of k_2 and the body wave arrival times. A bimodal distribution also emerges from the inferred models for the BML set considering the YM composition (Figure 2c3).

4.2. Contribution of All the Data Sets

The joint inversion of all three geophysical data sets leads to a substantial narrowing of the set of plausible models. The inferred joint posterior distribution of T_p and Mg# reveals distinct patterns. For the EH45 and TA compositions of the non-BML model set (Figures 1d1 and 1d2), the distribution of T_p and Mg# closely resemble those obtained from the inversion of the electrical conductivity data alone. However, models with Mg# values below 0.73 (EH45) and 0.755 (TA) are extremely unlikely, since predicted seismic wave arrival times and k_2 deviate significantly from the observed data. For EH45 and TA compositions, the posterior T_p-Mg# PDFs of the joint inversion are clearly subsets of those obtained with the separated inversion of the three data sets. For the YM composition (Figure 1d3), the shape of the inferred T_p-Mg# PDFs closely resembles that obtained using electrical conductivity data alone. The subset of models characterized by the PDF values was already present (albeit with smaller probability) in the individual inversions based on body wave arrival times and k_2 Love number. In the case of EH45 and TA compositions within the BML model set (Figures 2d1 and 2d2), the T_p-Mg# PDFs indicate that lower values of both parameters are significantly more probable than when using electrical conductivity data alone. This shift reflects the influence of seismic constraints, which favor models with cooler and more iron-rich mantle compositions. For the YM composition (Figure 2d3), the bimodal character of the posterior distribution, evident when inverting electrical conductivity data alone, is suppressed in the joint inversion. Specifically, the

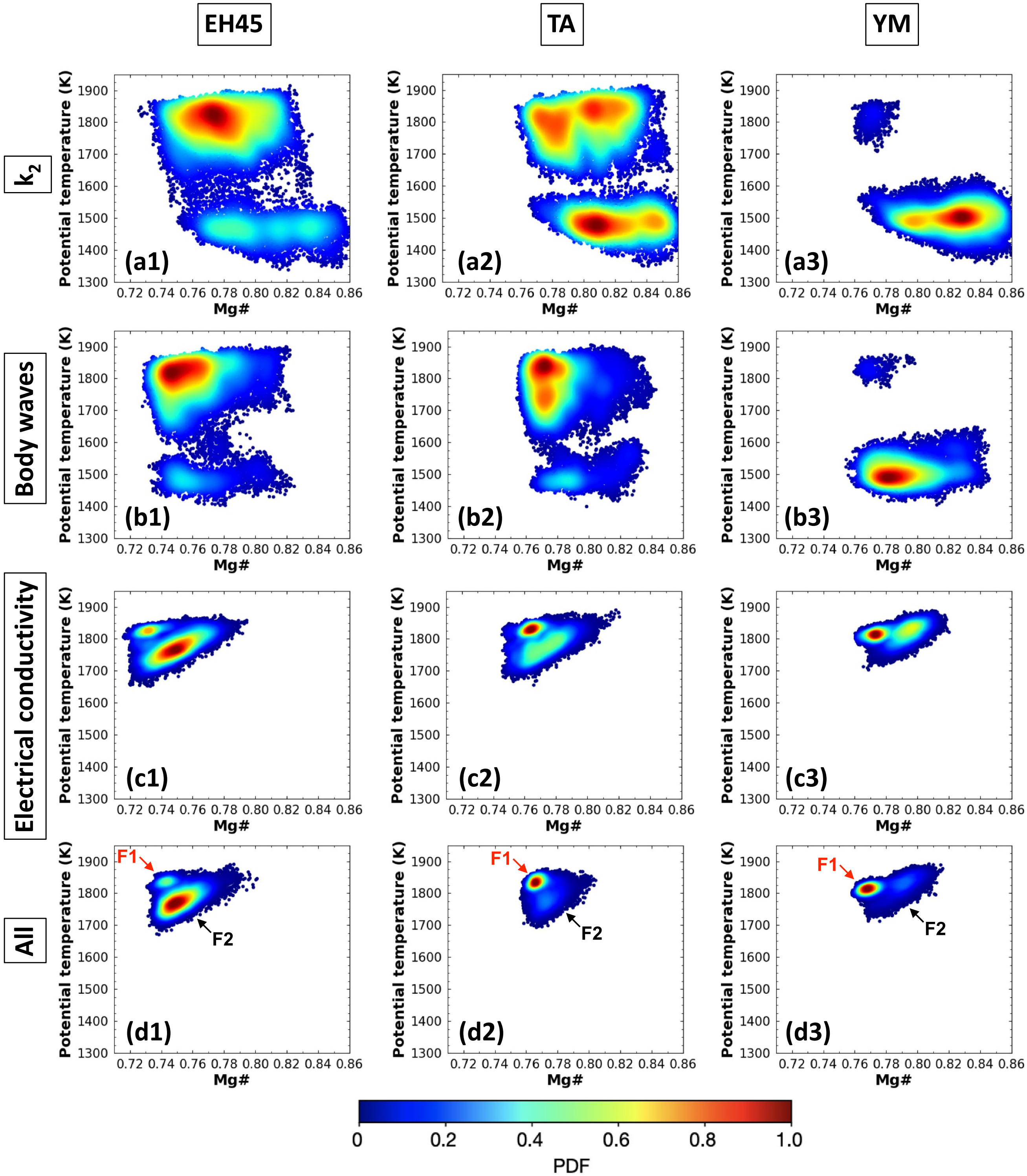

Figure 1. A posteriori probability density functions of the potential temperature as a function of Mg#, considering non-BML models. The inversion results using different data sets are shown in rows for k_2 (a1–a3), the body waves arrival times (b1–b2), the electrical conductivity (c1–c3), and the joint inversion of the three data sets (d1–d3). Each column corresponds to the results using a different composition: EH45, TA, and YM. Blue and red colors show small and large probabilities, respectively. In (d1–d3), the two families F1 (high-T_p, low-Mg#) and F2 (low-T_p, high-Mg#) are indicated with arrows.

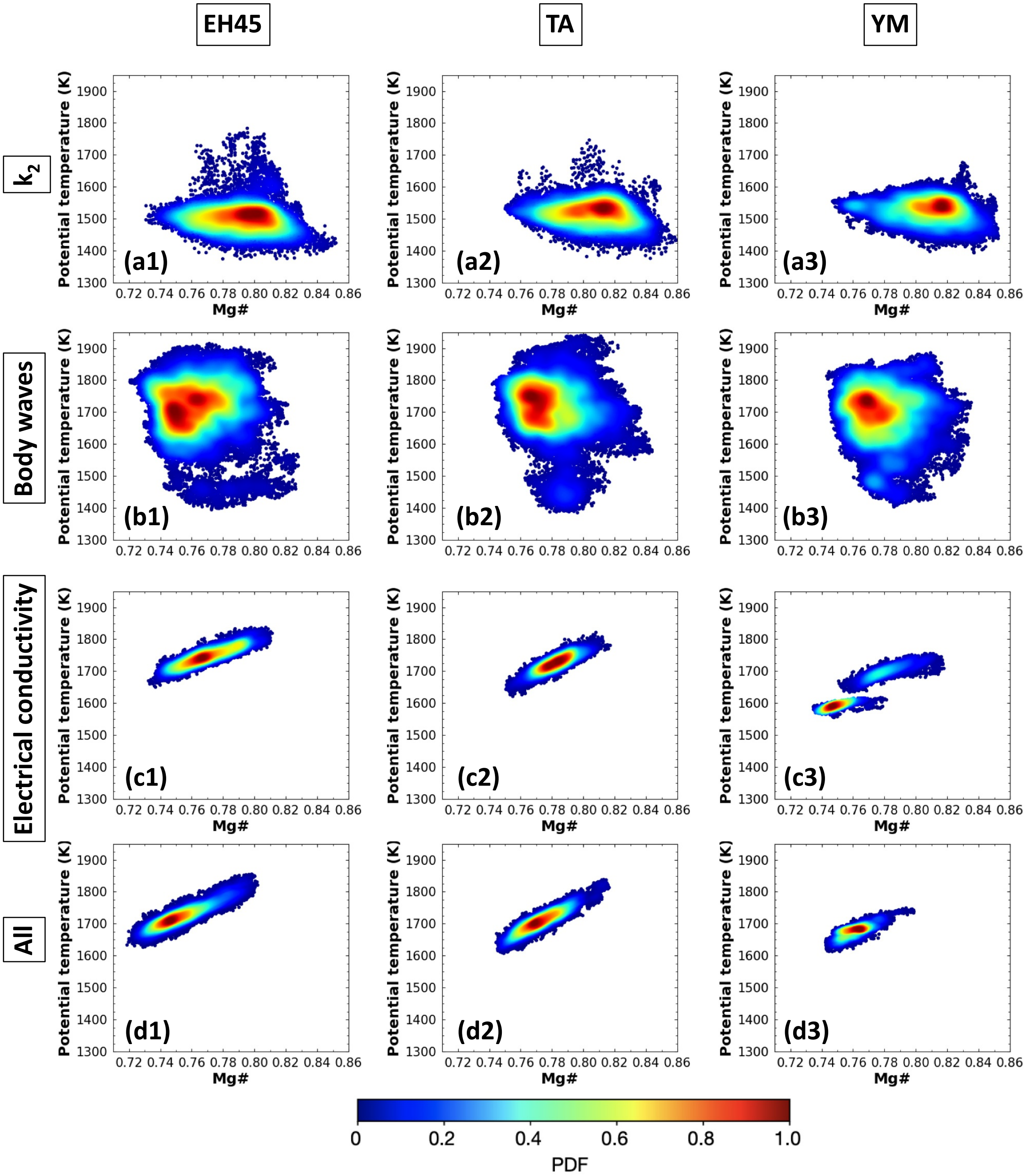

Figure 2. A posteriori probability density functions of the potential temperature as a function of Mg#, considering BML models. The inversion results using different data sets are shown in rows for k_2 (a1–a3), the body waves arrival times (b1–b3), the electrical conductivity (c1–c3), and the joint inversion of the three data sets (d1–d3). Each column corresponds to the results using a different composition: EH45, TA, and YM. Blue and red colors show small and large probabilities, respectively.

family of models characterized by $T_p < 1600$ K is no longer present, as it is incompatible with the k_2 Love number and with seismic data.

For each set of models (non-BML and BML for the three mantle compositions), the estimated mean values and standard deviations of geodynamical quantities are summarized in Table 3. For non-BML models exhibiting a bimodal T_p-Mg# distribution, the two distinct solution families, F1 and F2, are reported separately. Family F1 corresponds to models with larger T_p and smaller Mg# whereas family F2 includes models with smaller T_p and larger Mg#.

Compared to the previous findings of Samuel et al. (2023), which considered only the EH45 mantle composition, the mean values of the geodynamical parameters for our EH45-based F2 models fall within the error bars of the mean values reported by Samuel et al. (2023) (see their Table 1). However, the EH45-based F1 models differ significantly, with a mantle effective activation volume (V^*) larger by 4.9 cm^3/mol, an initial uppermost mantle temperature (T_{m_0}) higher by 56 K, a potential temperature (T_P) higher by 45 K, an uppermost mantle temperature increased (T_m) by 91 K, and a lithospheric and upper thermal boundary layer thickness (D_{lu}) greater by 276 km. For EH45-based BML models, compared to the supplementary set in Table 1 of Samuel et al. (2023), the thermal conductivity of the BML (k_d) is lower by 4.4 Wm^{-1} K^{-1}, T_P is 196 K larger, and D_{l_u} is 113 km thicker. The present-day temperatures at the CMB (T_c) and in the BML (T_d), are respectively ~800 K and ~500 K hotter than in Samuel et al. (2023). This arises from the fact that, in our current study, we adopted a minimum prior bound for the thermal conductivity in the BML (k_d) of 1 Wm^{-1} K^{-1}, compared to the value of 4 Wm^{-1} K^{-1} used in Samuel et al. (2023). Low k_d values are clearly favored in the inversion process, implying less efficient heat transfer and cooling, thereby resulting in higher present-day deep temperatures (Samuel et al., 2021) compared to the case with higher k_d values considered in Samuel et al. (2023).

4.3. Datafit

Figures 3 and 4 show the data fit estimates of the joint inversion for the non-BML and BML sets, respectively. The data fit for the inversion of the individual data sets are presented in Supporting Information S1 (Figures S1.1 and S1.2). Figure 3 shows that, for non-BML models, families F1 and F2 provide equally good fits to both the k_2 Love number and body wave arrival times. In contrast, electrical conductivity systematically yields smaller misfit values for F1 models, irrespective of the mantle composition. All three mantle compositions provide equally good fits to the k_2 Love number and seismic data (Figures 3a4 and 3b4). Since F1 models represent a significantly smaller subset of models, the total model ensemble for the EH45 composition, the electrical conductivity misfit distribution appears less favorable for EH45 compared to TA and YM (Figure 3c4). This discrepancy is also reflected in the overall misfit distribution (Figure 3d4), and is mainly driven by the k_2 Love number and seismic data, which are incompatible with models exhibiting Mg# < 0.73. When electrical conductivity data are inverted independently, the proportion of F1 models significantly increases for the EH45 composition (see Figure S1.1c1 in Supporting Information S1).

In the case of the BML set, models based on the three mantle compositions are all consistent with the observed k_2 Love number, falling within the associated uncertainty bounds (Figures 4a1–4a3). The misfit to electrical conductivity data is generally comparable and not dependent on the mantle composition (Figures 4c1–4c3), but remains noticeably larger than that obtained for the non-BML set (Figures 3c4 and 4c4), even when the electrical conductivity data are inverted individually (see Figures S1.1c4 and S1.2c4 in Supporting Information S1) The origin of this difference will be discussed in the subsequent section (Section 4.4). In contrast to the EH45 and TA-based BML models, which produce misfit values for body wave arrival times similar to those of the non-BML models, the YM-based BML models exhibit larger misfits with respect to the seismic observations (Figure 4b4). When seismic data are inverted alone assuming the YM mantle composition, the resulting fit improves and becomes comparable to those obtained with the EH45 and TA compositions (see Figure S1.2b4 in Supporting Information S1). To achieve compatibility with the various geophysical data sets in the joint inversion, the fit to the seismic data is slightly degraded for YM-based models. Compared to the non-BML set, the poorer fit of the BML set to the electrical conductivity data leads to a larger overall misfit (Figures 3d4 and 4d4), an effect that is even more pronounced for models based on the YM composition.

Table 3
Summary of the Inversion Results

Inverted parameter	Meaning	EH45		TA		YM		EH45	TA	YM	Units
		Non-BML		Non-BML		Non-BML		BML	BML	BML	
		F1 (16%)	F2 (84%)	F1 (61%)	F2 (39%)	F1 (44%)	F2 (56%)				
E^*	Mantle effective activation energy*	303 ± 38	323 ± 78	288 ± 23	315 ± 55	287 ± 31	280 ± 91	176 ± 68	150 ± 38	153 ± 83	kJ/mol
V^*	Mantle effective activation volume*	9.5 ± 0.5	6.4 ± 2.5	9.5 ± 0.4	7.6 ± 2.1	9.4 ± 0.4	4.9 ± 2.8	5.6 ± 2.5	5.6 ± 2.3	8.2 ± 1.5	$\mathrm{cm^3/mol}$
η_0	Mantle reference viscosity*	$10^{22.2\pm0.2}$	$10^{21.8\pm0.3}$	$10^{22.2\pm0.1}$	$10^{21.8\pm0.2}$	$10^{22.1\pm0.1}$	$10^{22.3\pm0.3}$	$10^{21.2\pm0.4}$	$10^{21.3\pm0.3}$	$10^{20.9\pm0.5}$	Pa s
T_{m_0}	Initial uppermost mantle temperature*	1,806 ± 41	1,754 ± 33	1,793 ± 41	1,761 ± 36	1,712 ± 10	1,715 ± 13	1,750 ± 55	1,724 ± 18	1,822 ± 109	K
T_{c_0}	Initial CMB temperature*	2,275 ± 80	2,196 ± 75	2,249 ± 69	2,207 ± 75	2,064 ± 28	2,069 ± 53	2,184 ± 88	2,166 ± 77	2,261 ± 127	K
R_c	Core radius*	1,815 ± 22	1,820 ± 23	1,821 ± 24	1,830 ± 26	1,835 ± 21	1,838 ± 21	1,659 ± 38	1,656 ± 43	1,638 ± 48	km
K_S	Core isentropic bulk modulus at CMB*	146 ± 11	143 ± 10	151 ± 11	147 ± 11	148 ± 11	147 ± 11	150 ± 11	156 ± 12	159 ± 12	GPa
K'_S	Pressure derivative of K_S *	4.0 ± 1.2	4.0 ± 1.2	3.7 ± 1.1	3.9 ± 1.1	4.0 ± 1.3	4.0 ± 1.2	4.5 ± 1.2	4.6 ± 1.1	4.5 ± 1.3	-
k_d	BML thermal conductivity	-	-	-	-	-	-	1.6 ± 0.5	1.6 ± 0.5	4.0 ± 3.5	$\mathrm{Wm^{-1}\ K^{-1}}$
D_d	BML thickness	-	-	-	-	-	-	162 ± 33	160 ± 46	200 ± 55	km
Mg#	Mg number	0.744 ± 0.005	0.753 ± 0.009	0.767 ± 0.004	0.775 ± 0.007	0.768 ± 0.003	0.780 ± 0.001	0.755 ± 0.016	0.773 ± 0.012	0.753 ± 0.010	-

Output parameter	Meaning	EH45		TA		YM		EH45	TA	YM	Units
		Non-BML		Non-BML		Non-BML		BML	BML	BML	
		F1	F2	F1	F2	F1	F2				
T_p	Potential temperature	1,835 ± 14	1,780 ± 29	1,835 ± 15	1,785 ± 30	1,815 ± 10	1,818 ± 27	1,726 ± 37	1,708 ± 35	1,632 ± 44	K
T_m	Uppermost mantle temperature	1,971 ± 20	1,871 ± 38	1,974 ± 20	1,883 ± 40	1,945 ± 13	1,916 ± 33	1,778 ± 42	1,756 ± 38	1,668 ± 50	K
T_c	CMB temperature	2,166 ± 30	2,083 ± 40	2,166 ± 30	2,104 ± 43	2,069 ± 16	2,098 ± 32	3,437 ± 201	3,497 ± 272	3,521 ± 724	K
D_{cr}	Crustal thickness	70.6 ± 1.2	69.2 ± 2.2	70.8 ± 0.9	70.1 ± 1.5	71.7 ± 0.3	71.2 ± 0.8	66.6 ± 4.5	67.5 ± 4.2	70.0 ± 2.2	km
D_{lu}	Lithospheric and upper TBL thickness	876 ± 45	611 ± 66	898 ± 45	653 ± 78	852 ± 32	644 ± 88	363 ± 33	334 ± 24	266 ± 41	km
ρ_{CMB}	Core density at CMB	5,855 ± 66	5,855 ± 72	5,858 ± 74	5,843 ± 81	5,811 ± 57	5,848 ± 80	5,932 ± 593	6,054 ± 546	5,186 ± 553	$\mathrm{kg/m^3}$
ρ_c	Average core density	6,110 ± 61	6,117 ± 71	6,108 ± 71	6,099 ± 79	6,062 ± 54	6,106 ± 79	6,500 ± 129	6,531 ± 159	6,455 ± 167	$\mathrm{kg/m^3}$
F_s	Surface heat flux	20.9 ± 0.4	21.4 ± 0.3	21.9 ± 0.2	22.4 ± 0.3	23.7 ± 0.1	24.3 ± 0.4	19.2 ± 0.6	20.5 ± 0.7	23.2 ± 0.2	$\mathrm{mW/m^2}$
dT_l/dr	Lithospheric thermal gradient	1.72 ± 0.04	1.88 ± 0.08	1.69 ± 0.03	1.79 ± 0.06	1.59 ± 0.01	1.65 ± 0.1	2.64 ± 0.19	2.56 ± 0.21	1.95 ± 0.71	K/km
P_c	Pressure at CMB	19.2 ± 0.3	19.1 ± 0.3	19.1 ± 0.3	19.0 ± 0.3	18.9 ± 0.3	18.8 ± 0.3	21.4 ± 0.5	21.4 ± 0.6	21.7 ± 0.6	GPa
T_d	Average BML temperature	-	-	-	-	-	-	3,051 ± 204	3,105 ± 291	3,175 ± 730	K

Note. Quantities listed correspond to constant or to present-day mean values and 1-σ uncertainty unless specified otherwise. The superscripts "$\star$" indicate the input parameters of our geodynamical model, that we vary in the inversion algorithm (top). The other parameters are derived from the input parameters and the geodynamical modeling (bottom). The subscripts "0" indicate initial values for quantities that vary in time. Given the emergence of a bimodal solution for the non-BML set, the characteristics of each solution (F1 and F2) are presented separately. Family F1 corresponds to models with larger T_p and smaller Mg# values. The proportion of models associated with each family is also reported in %.

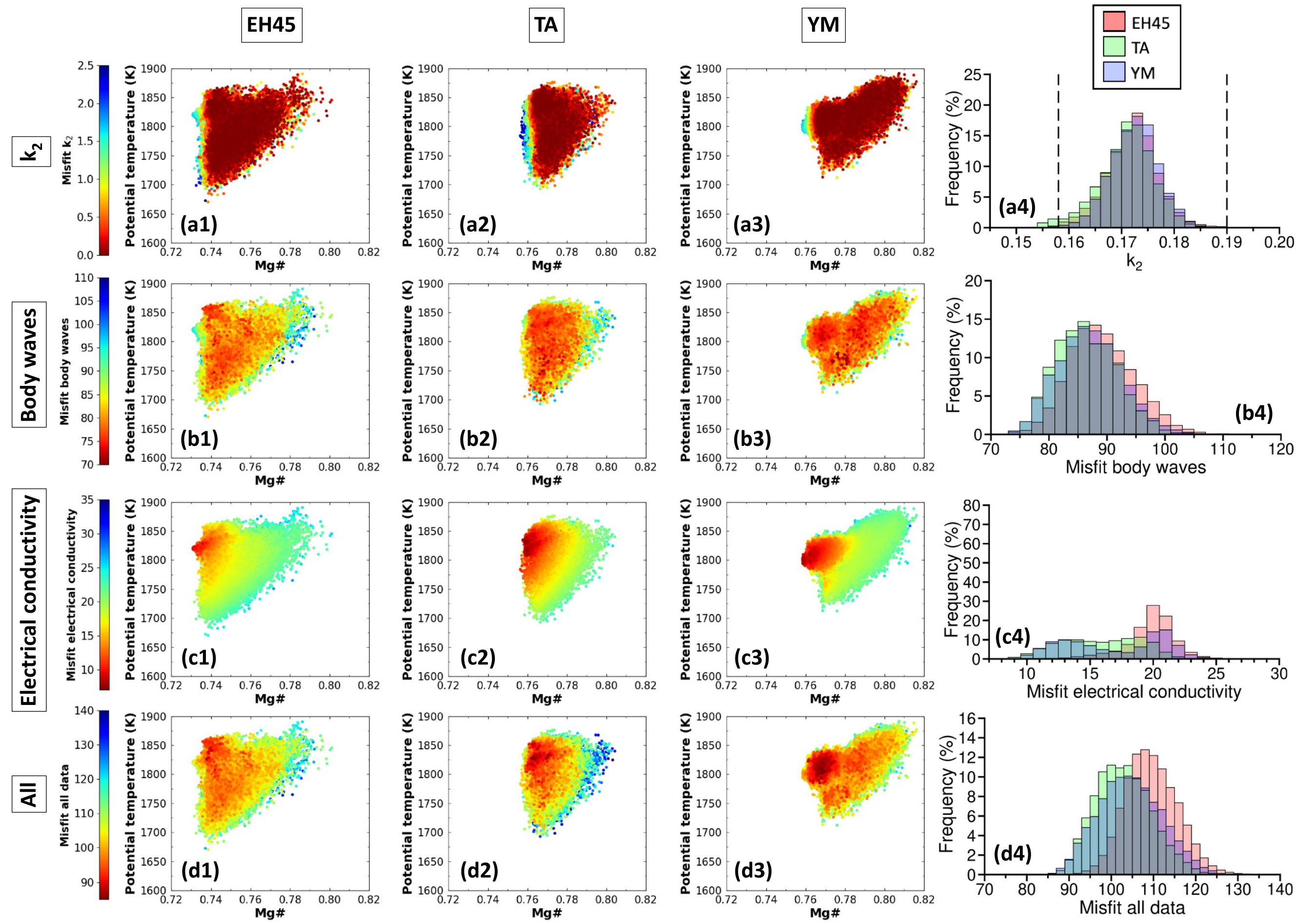

Figure 3. Data fit estimates of the joint inversion for the non-BML set. The first three columns show T_p as a function of Mg# for the three compositions. In panels (a1–a3), (b1–b3), (c1–c3), and (d1–d3), the color refers to the misfit value estimated for k_2, the body wave arrival times, the electrical conductivity, and all three data sets, respectively. Red and blue colors are small and large misfit values, respectively. (a4) Shows the k_2 distribution. The black dashed lines show the 2σ uncertainty around the value of Konopliv et al. (2020) ($k_2 = 0.174 \pm 0.016$). Panels (b4, c4) display the misfit distributions of body wave arrival times and electrical conductivity, respectively. (d4) Shows the distribution of the total misfit value of the three data sets (Equation 3). In panels (a4–d4), the distributions considering EH45, TA, and YM compositions are displayed in red, green, and blue, respectively.

4.4. Temperature and Electrical Conductivity Profiles

The output temperature and electrical conductivity profiles from the joint inversion are presented in Figures 5 and 6 for the non-BML and BML models, respectively. The same figures, showing the inversion outputs based on electrical conductivity data only, are presented in Section S2 of Supporting Information S1.

For non-BML models, the two solutions F1 and F2 are clearly associated with distinct shapes of temperature and electrical conductivity profiles (Figure 5). In particular, F1 models are characterized by thicker lithospheric and upper thermal boundary layers (D_{lu}) compared to F2 models, with values exceeding 800 km (Table 3 and Figures 5a–5c). In contrast, most F2 models exhibit D_{lu} values ranging between 550 and 750 km. The temperature profiles associated with the BML models show even smaller D_{lu} values compared to the F2 models, with values ranging between 250 and 350 km (Table 3 and Figures 6a–6c). In contrast to the non-BML temperature profiles, which are well positioned below the solidus of Duncan et al. (2018), the solidus plays a major role in constraining the BML temperature profiles by limiting the formation of thin D_{lu}. While certain output temperature profiles in Figures 5a–5c and 6a–6c appear to intersect the solidus curve from Duncan et al. (2018), which is shown for a fixed Mg# of 0.75, this apparent crossing is misleading. As detailed in Section 3.1.2, the solidus temperature is composition-dependent and varies with Mg#, meaning that each model has its own corresponding solidus curve (following the parameterization used in Section 4.2 in Samuel et al. (2021)) that is not explicitly shown here. As

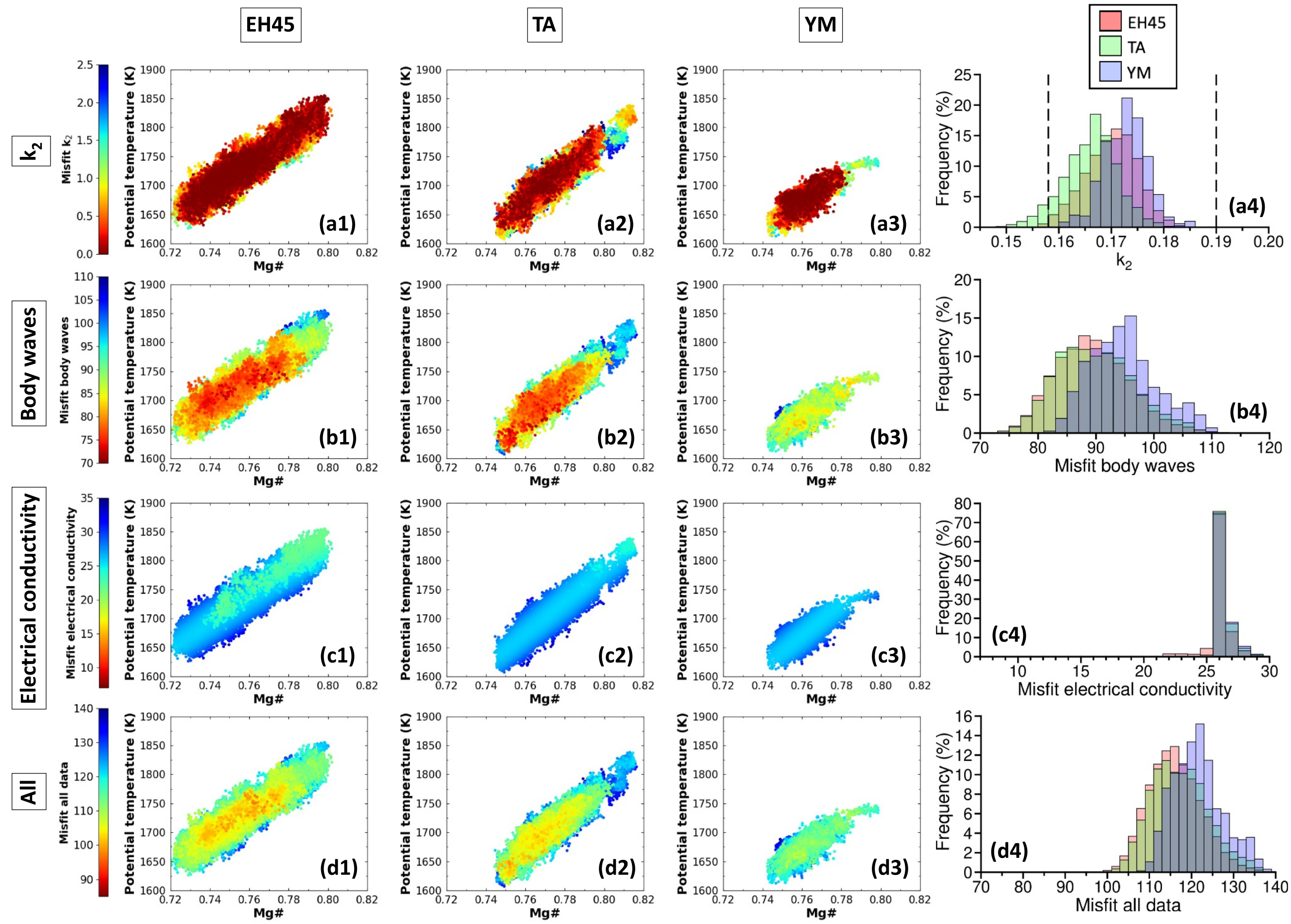

Figure 4. Data fit estimates of the joint inversion for the BML set. The first three columns show T_p as a function of Mg# for the three compositions. In panels (a1–a3), (b1–b3), (c1–c3), and (d1–d3), the color refers to the misfit value estimated for k_2, the body wave arrival times, the electrical conductivity, and all three data sets, respectively. Red and blue colors are small and large misfit values, respectively. (a4) Shows the k_2 distribution. The black dashed lines show the 2σ uncertainty around the value of Konopliv et al. (2020) ($k_2 = 0.174 \pm 0.016$). Panels (b4, c4) display the misfit distributions of body wave arrival times and electrical conductivity, respectively. (d4) Shows the distribution of the total misfit value of the three data sets (Equation 3). In panels (a4–d4), the distributions considering EH45, TA, and YM compositions are displayed in red, green, and blue, respectively.

seen in Samuel et al. (2023), the initially hotter mantle, but now colder in the present day, results in thinner present-day lithospheres for the BML sets (Samuel et al., 2023). These differences between initial and present-day mantle temperatures are larger if the mantle compositions are TA or YM (which both contain more HPEs) than for the EH45 composition, resulting in even thinner lithospheres compared to non-BML sets.

For the non-BML set, the distinct temperature profile shapes of F1 and F2 models are clearly reflected in the corresponding output electrical conductivity profiles (Figures 5d–5f). In the uppermost thermal boundary layer, the F1 electrical conductivity profiles closely reproduce the slope of the conductivity profile proposed by Civet and Tarits (2014). The electrical conductivity profiles of F2 are steeper than those of F1, which explains their poorer fit to the conductivity data compared to F1 profiles (Figures 3c1–3c4). The BML models that best fit the data exhibit thin D_{lu} layers, indicating that their temperature profiles between 400 and 900 km depth are primarily governed by the mantle temperature. Consequently, the resulting electrical conductivity profiles are even more vertically oriented than those of the F2 models from the non-BML set (Figures 6d–6f), which accounts for their poorer fit to the conductivity data compared to the non-BML models (Figures 3c4 and 4c4).

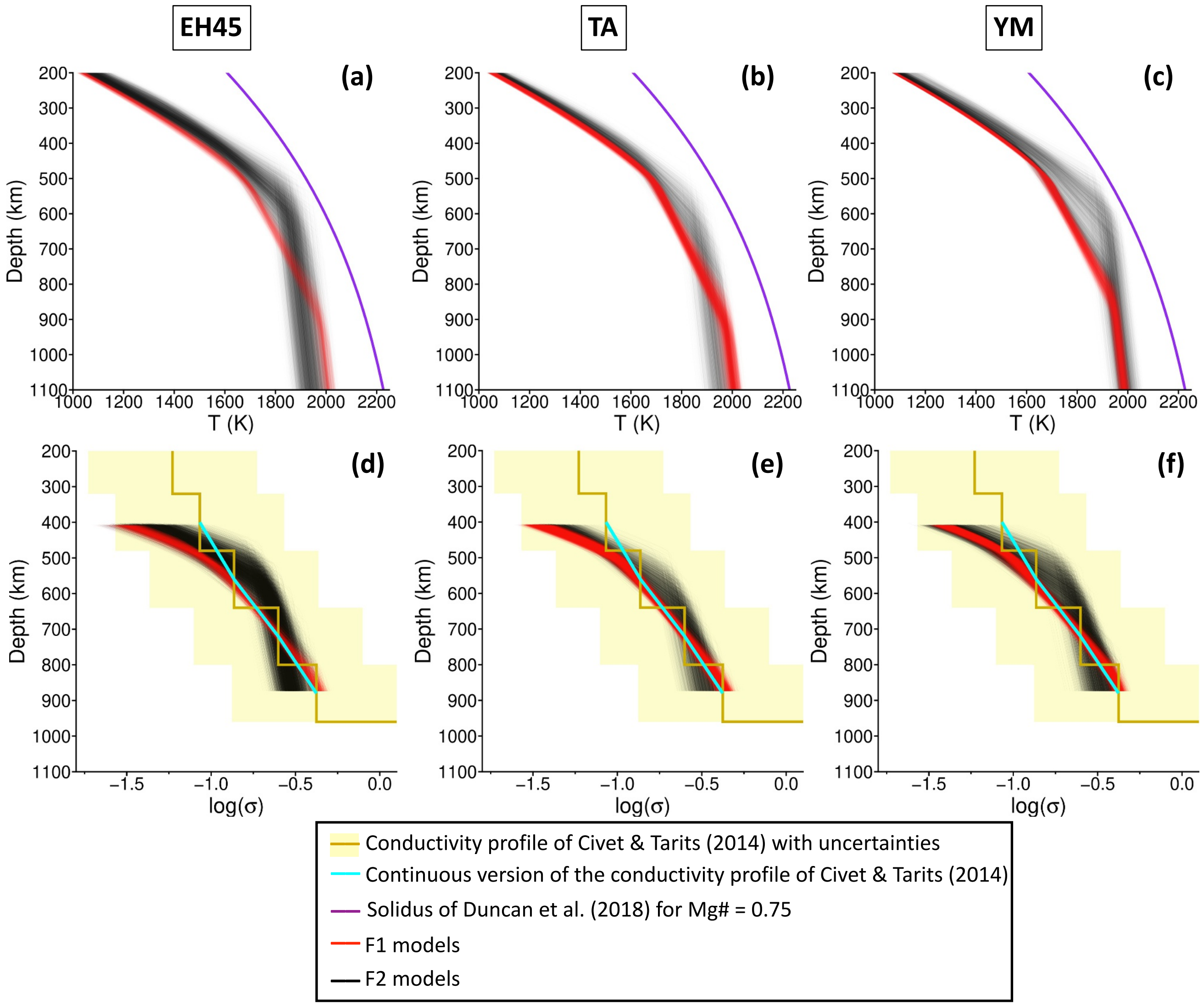

Figure 5. Temperature and electrical conductivity output profiles for the non-BML set. Panels (a–c) display the output temperature profiles, while panels (d–f) show the output electrical conductivity profiles for the three compositions. In panels (a–c), the solidus from Duncan et al. (2018) estimated for Mg# = 0.75 is shown in purple. In panels (d–f), the electrical conductivity profile from Civet and Tarits (2014) is shown in khaki, with its uncertainties represented in yellow. The continuous version of the Civet and Tarits (2014) conductivity profile (see Section 2), to which the synthetic conductivity profiles are compared in the inversion, is depicted in cyan. The output profiles for families F1 and F2 are represented in red and black, respectively. The output electrical conductivity profiles are shown only between 400 and 900 km depth, as this is the range over which they are compared with the continuous version of the conductivity profile from Civet and Tarits (2014).

4.5. Seismic Profiles

The V_P and V_S velocity profiles predicted from the model parameters inferred from the joint inversion are presented in Figures 7 and 8 for the non-BML and BML sets, respectively. In order to better evaluate the impact of the joint inversion, the output velocity profiles obtained from the inversion of body wave arrival times alone are also shown. The joint inversion significantly constrains the range of acceptable velocity models. Although the differential body wave arrival times we use in this study are not directly sensitive to the depth at which the main mineralogical phase transitions occur, the reduced uncertainty of the inferred temperature profiles narrows down the possible depth range of these transitions. In the non-BML F2 and BML models (Figures 7 and 8), two discontinuities occur close to a depth of 1,000 km. The shallower discontinuity results from the transition of orthopyroxene to high-pressure clinopyroxene and the deeper transition, which results in a larger velocity jump, from the transition of olivine to wadsleyite. In the non-BML F1 models (Figures 5a and 5b), both phase transitions occur at similar depths, causing their seismic signatures to merge into a single, combined discontinuity. Owing to

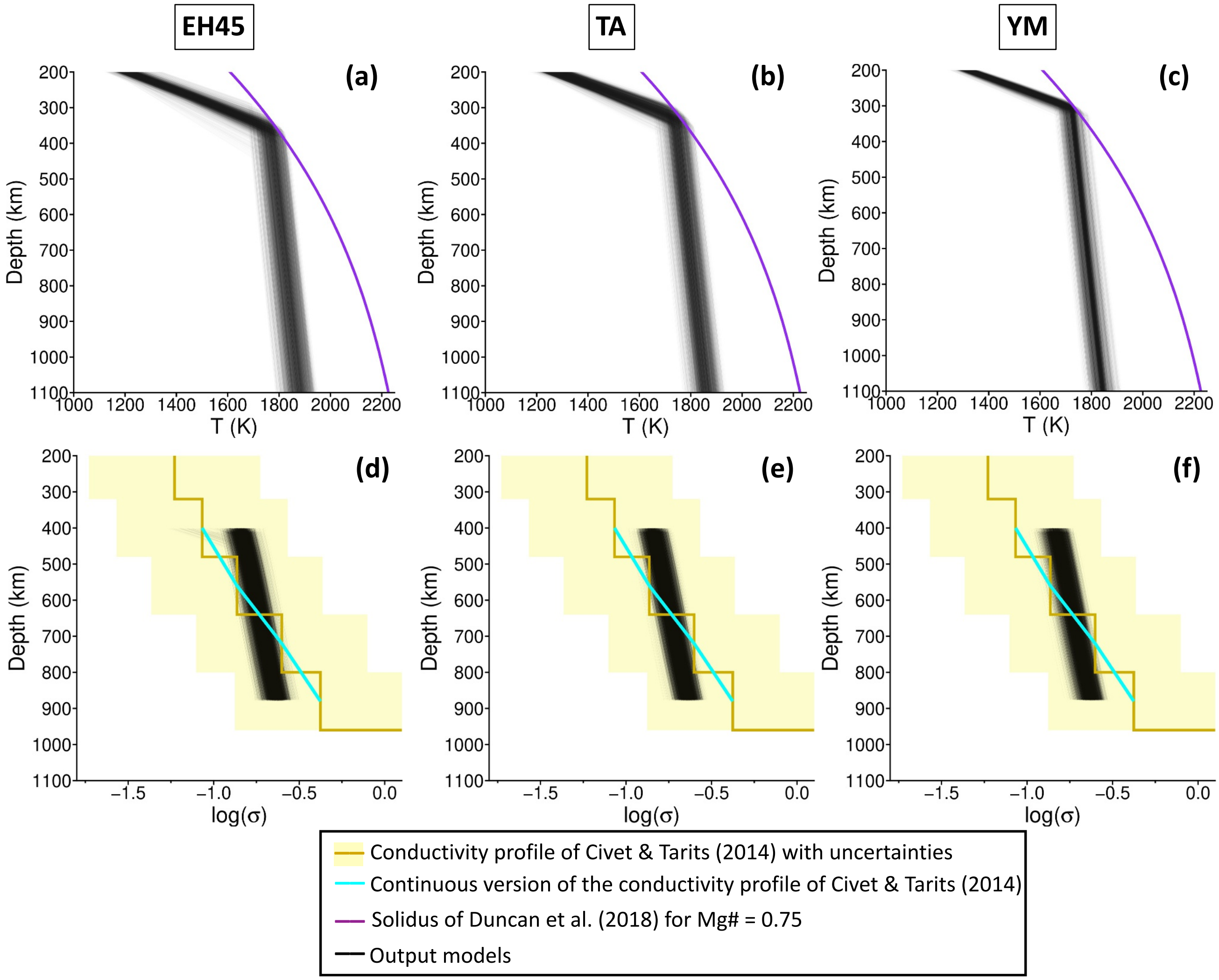

Figure 6. Temperature and electrical conductivity output profiles for the BML set. Panels (a–c) display the output temperature profiles, while panels (d–f) show the output electrical conductivity profiles for the three compositions. In panels (a–c), the solidus from Duncan et al. (2018) estimated for Mg# = 0.75 is shown in purple. In panels (d–f), the electrical conductivity profile from Civet and Tarits (2014) is shown in khaki, with its uncertainties represented in yellow. The continuous version of the Civet and Tarits (2014) conductivity profile (see Section 2), to which the synthetic conductivity profiles are compared in the inversion, is depicted in cyan. The output profiles are represented in black. The output electrical conductivity profiles are shown only between 400 and 900 km depth, as this is the range over which they are compared with the continuous version of the conductivity profile from Civet and Tarits (2014).

the exothermic nature of the two mineralogical phase transitions and the higher temperatures below 900 km in non-BML F1 models (Figures 5a and 5b) compared to non-BML F2 and BML models, these transitions occur at greater depths in the non-BML F1 case. The different mineralogical phase proportions as a function of depth are further discussed in Section 5.1.

Using observed triplicated *P* and *S* waves from five teleseismic events and considering non-BML models, Huang et al. (2022) constrained the depth of a sharp seismic discontinuity in the Martian mantle to 1,006 ± 40 km and associated it with the olivine to wadsleyite transition. Among the tested mantle compositions, Huang et al. (2022) demonstrated that only models based on the EH45 mantle composition have a discontinuity at a depth consistent with their estimate. Assuming that the 1,006 ± 40 km value corresponds to the mid-point of the transition, we reach the same conclusion as Huang et al. (2022): some of our EH45 models fall within the uncertainty range, while none of the TA or YM models do. In contrast, for models with a BML, the mid-depth of the olivine to wadsleyite transition occurs at depths of 1,006 ± 40 km in nearly all cases, regardless of the assumed mantle composition.

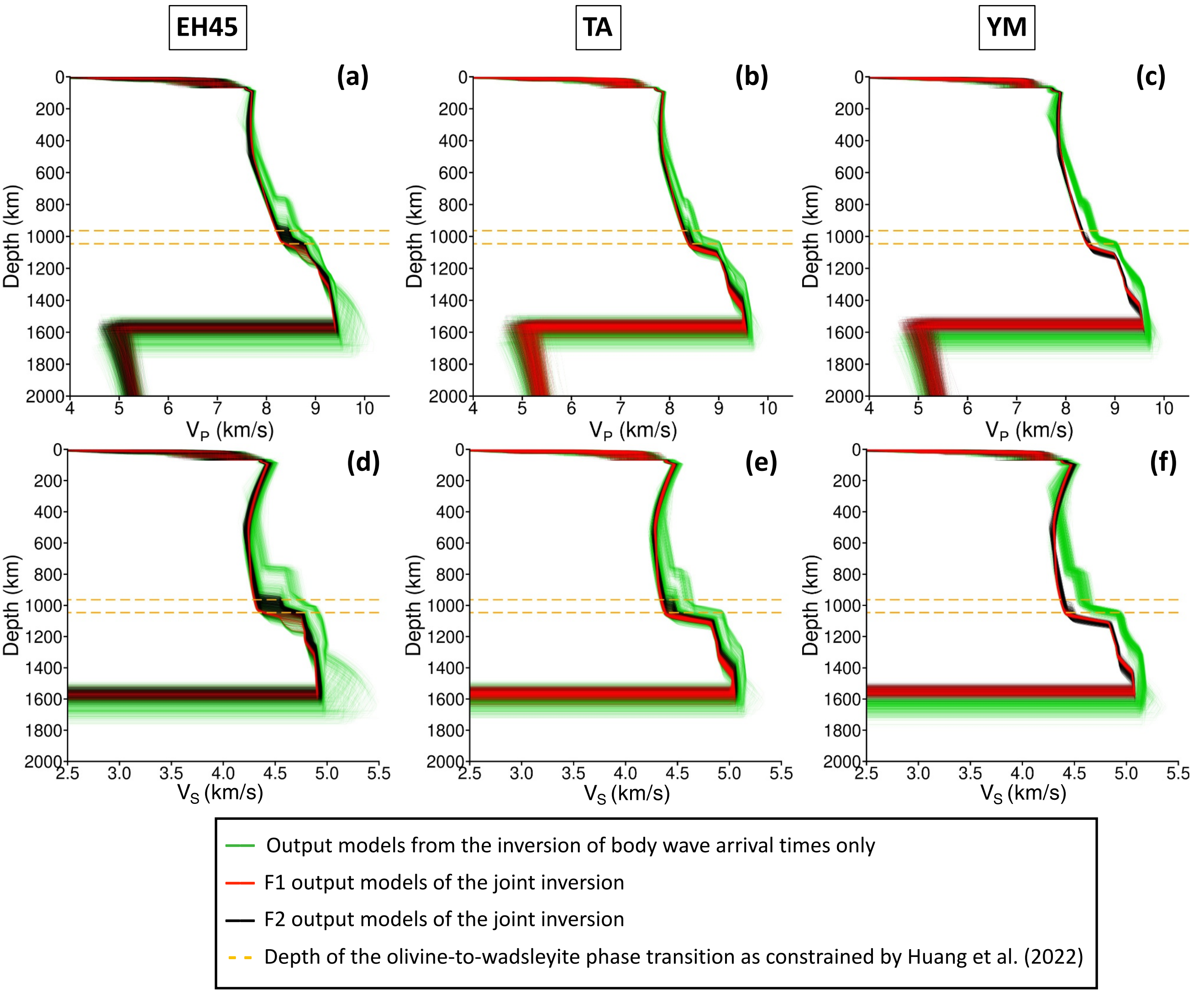

Figure 7. Output V_P (a–c) and V_S (d–f) profiles for the three compositions, considering the non-BML set. The results obtained from the inversion of body wave arrival times alone are shown in green. For the joint inversion, the velocity profiles corresponding to families F1 and F2 are displayed in red and black, respectively. The uncertainties in the depth of the olivine to wadsleyite phase transition, as constrained by Huang et al. (2022), are represented by dashed orange lines (1,006 ± 40 km).

For the non-BML set, the estimated core radii are relatively similar (~1,820 km) whatever the mantle composition considered, in good agreement with previous studies (Drilleau et al., 2022; Durán et al., 2022; Irving et al., 2023; Stähler et al., 2021). As shown by Samuel et al. (2023) for the EH45 mantle composition, and further supported by our current study using the TA and YM compositions, none of these models can reproduce the abnormally slow P wave signals diffracted along the core–mantle boundary recorded on sol 1,000 (see Figure S3.1 in Supporting Information S1). Both EH45 and TA BML models successfully reproduce the arrival times of core-sensitive seismic phases, including the two SKS phases (Irving et al., 2023) recorded on sols 976 and 1,000, and the P wave diffracted at the boundary between the BML and the core. For these two mantle compositions, the thickness of the BML (D_d) is approximately 160 km (Table 3), which falls within the uncertainty range of values estimated by Samuel et al. (2023). In contrast, the BML thickness is on average ~40 km larger when using the YM mantle composition. However, these models produce a poorer fit to the P-diffracted wave compared to those based on EH45 and TA (see Figure S3.1 in Supporting Information S1).

Given that only a single seismic station is available on Mars, there exists an inherent trade-off between seismic velocity models and the inferred source locations. An illustration of how epicentral distances vary with the

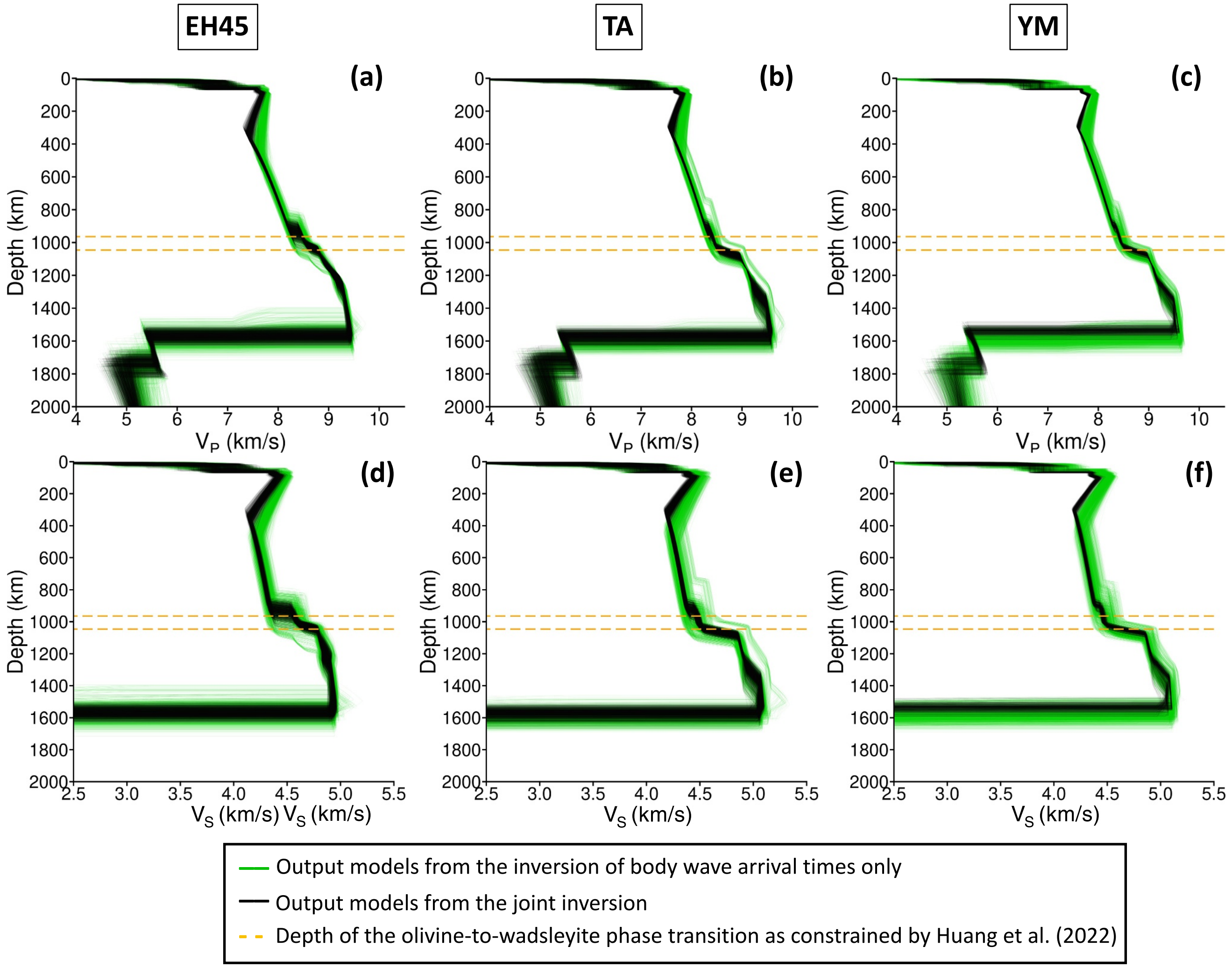

Figure 8. Output V_P (a–c) and V_S (d–f) profiles for the three compositions, considering the BML set. The results obtained from the inversion of body wave arrival times alone are shown in green. The output velocity profiles of the joint inversion are displayed black. The uncertainties in the depth of the olivine to wadsleyite phase transition, as constrained by Huang et al. (2022), are represented by dashed orange lines (1,006 ± 40 km).

seismic velocity model is shown in Figure S4.1 in Supporting Information S1. The results indicate that, across the different mantle compositions, the mean differences in epicentral distance are up to 1 and 3° for non-BML and BML models, respectively.

Using our output models, we determined the attenuation structure of Mars at seismic frequency (1 Hz) that one would obtain if the global attenuation at Phobos tidal frequency lied withing the range 95 ± 10 (Khan et al., 2018; Pou et al., 2022). This investigation showed that hotter non-BML models with low frequency dependence of attenuation systematically exhibit strong seismic attenuation that is beyond minimum bounds recently inferred for Mars' solid mantle at seismic frequency (Li et al., 2025) (Figure S5.1 in Supporting Information S1).

5. Discussion

5.1. Influence of the Thermodynamical Database

Thanks to thermodynamic modeling, it is now possible to compute mantle phase equilibria and physical properties across the entire pressure–temperature space for compositions with an arbitrary number of components and phases. This method is particularly valuable when interpreting sparse planetary geophysical data sets, as those used in our study. To date, all interior models derived from InSight seismic data rely on the thermodynamic

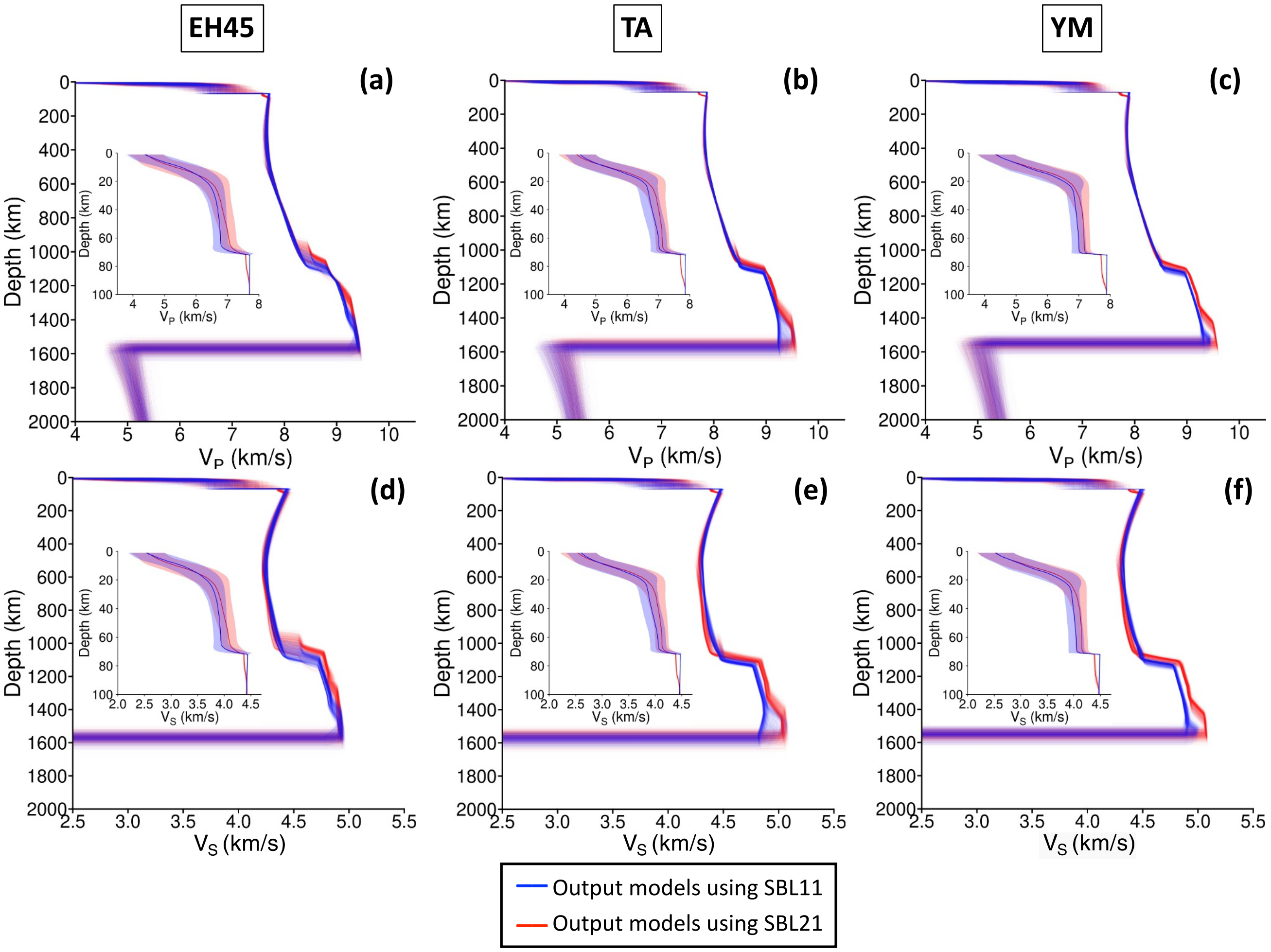

Figure 9. Output V_P (a–c) and V_S (d–f) profiles for the three compositions, considering the non-BML set, using SLB11 (in blue) and SLB21 (in red). The insets display the mean crustal velocity profiles along with their associated uncertainties.

database of Stixrude and Lithgow-Bertelloni (2011), including the models of for example, Drilleau et al. (2022, 2024), Durán et al. (2022), Huang et al. (2022), Irving et al. (2023), Khan et al. (2021), Samuel et al. (2023), and Stähler et al. (2021). In this study, we used the more recent thermodynamic database of Stixrude and Lithgow-Bertelloni (2021).

To investigate how the choice of the thermodynamic database could influence our results, we re-ran our joint inversion algorithm using the Stixrude and Lithgow-Bertelloni (2011) database instead of the more recent Stixrude and Lithgow-Bertelloni (2021) (hereafter referred to as SBL11 and SLB21). Using SBL11, Figures S6.1 and S6.2 in Supporting Information S1 show that the resulting distributions of T_p and Mg# are very similar to those obtained with SLB21, and that the datafit remains comparable to that presented in Figures 1 and 2 using SLB21, both for non-BML and BML models.

However, the seismic velocity profiles obtained with SLB11 differ significantly from those based on SLB21, both for non-BML and BML models (Figures 9 and 10). Regardless of the composition of the mantle and presence of a BML, the use of SLB21 introduces an additional discontinuity below the Moho, at approximately 80 km depth, which is absent in the models generated with SLB11. The estimated mean crustal velocities are also systematically higher when using SLB21 compared to SLB11 (see insets in Figures 9 and 10). Furthermore, the location and amplitude of seismic discontinuities or velocity gradients associated with mineralogical phase transitions, ranging from a depth of ∼900 km down to the core or the BML, differ significantly between the two

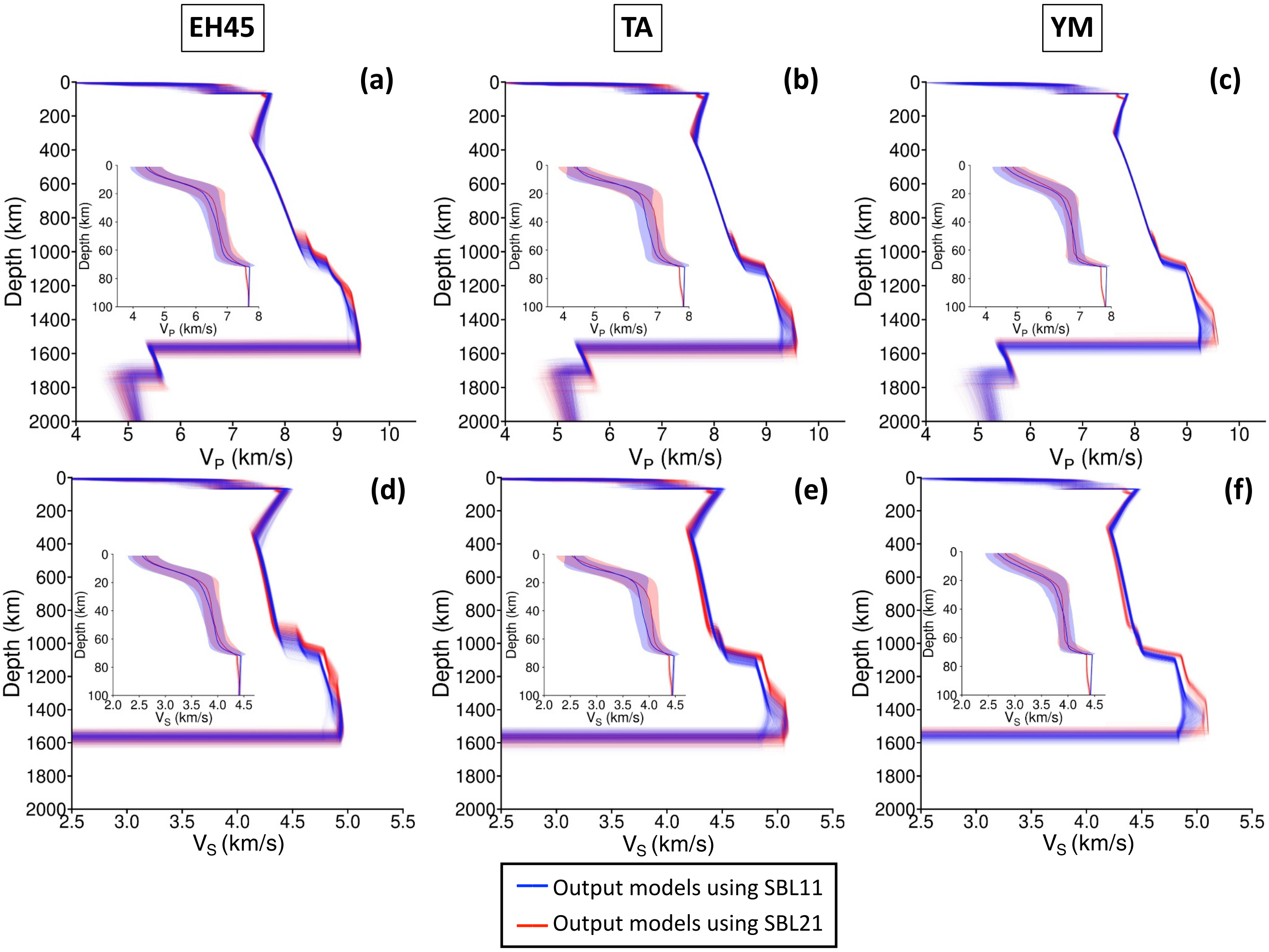

Figure 10. Output V_P (a–c) and V_S (d–f) profiles for the three compositions, considering the BML set, using SLB11 (in blue) and SLB21 (in red). The insets display the mean crustal velocity profiles along with their associated uncertainties.

thermodynamic databases. In particular, when using SLB11 instead of SLB21, these discontinuities or gradients are consistently shifted to greater depths, and the seismic velocities at the base of the mantle are notably smaller.

To better identify the minerals responsible for these differences, we selected a representative temperature profile and Mg# for each mantle composition from the best-fitting models, and computed the corresponding seismic velocity profiles and phase diagrams using both SLB11 and SLB21. Figures 11 and 12 show in columns (d) that the seismic discontinuity observed at approximately 80 km depth in models based on SLB21 results from the mineralogical transformation of spinel and feldspar into garnet. In contrast, spinel and feldspar are absent when using SLB11 (columns (c) in Figures 11 and 12). Another feature common to all models, regardless of mantle composition, is that the proportion of clinopyroxene is smaller with SLB21 compared to SLB11, in favor of orthopyroxene. While this has a relatively minor effect on V_P, it systematically reduces V_S between approximately 200 and 900 km depth. The proportion of high-pressure clinopyroxene is smaller when using SLB11 compared to SLB21, and even disappears entirely in TA- and YM-based non-BML models (Figures 11c2 and 11c3). Below 900 km depth, clinopyroxene remains stable to greater depths in SLB11-based models than in those using SLB21, which contributes to the smaller seismic velocities. These smaller velocities are also explained by the greater proportion of ferropericlase in the deep mantle when using SLB11, whereas ferropericlase is often absent or present in only small amounts with SLB21. The absence of ringwoodite in some cases based on SLB11 (Figures 11c2 and 12c3) further increases the seismic velocity differences between SLB11 and SLB21.

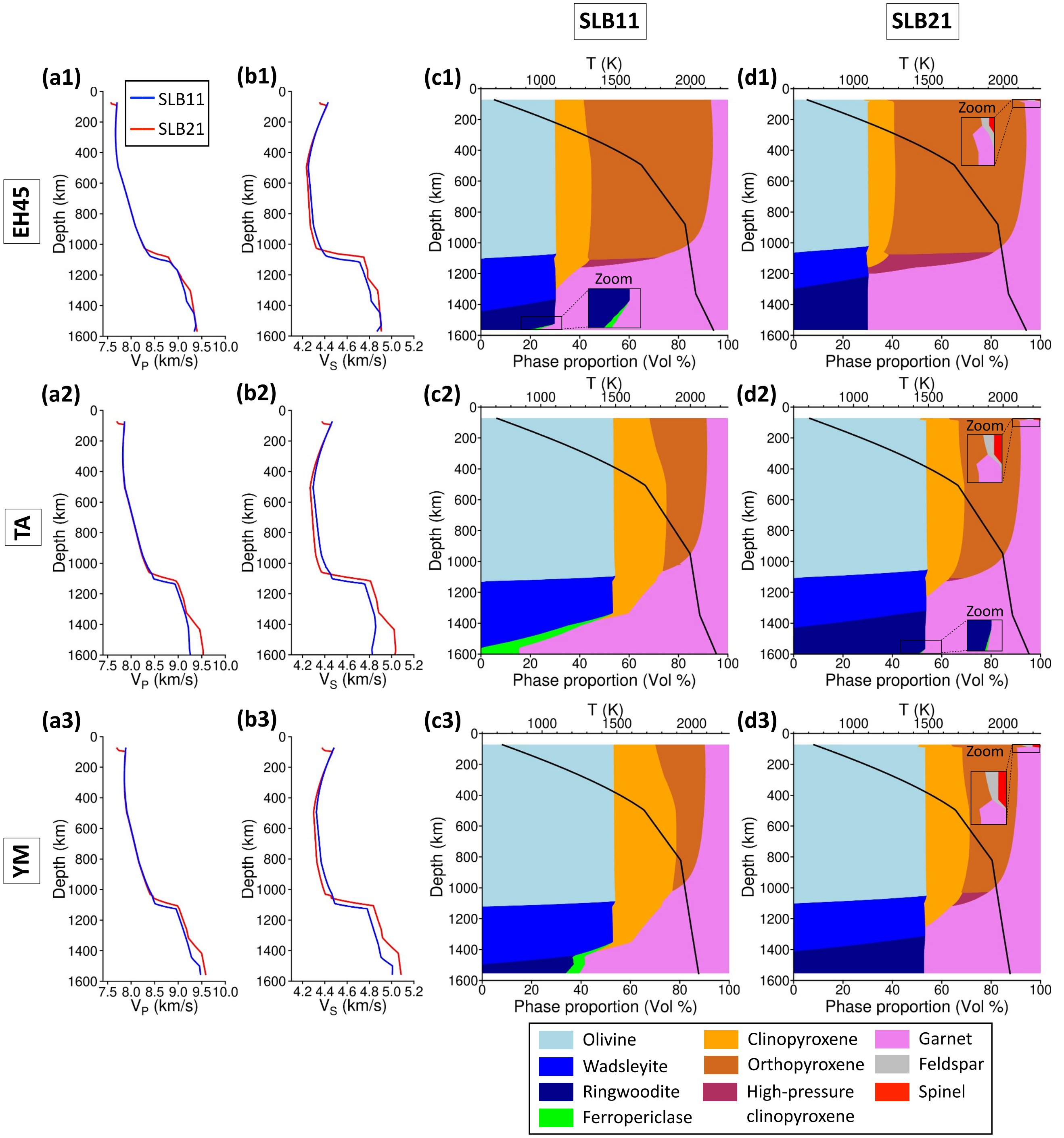

Figure 11. Comparison of seismic velocities and mineralogical phase diagrams between SLB11 and SLB21 for non-BML models, using a given temperature profile and Mg#. The three rows present results for the EH45, TA, and YM mantle compositions. Panels (a1–a3) and (b1–b3) display the output V_P and V_S profiles in the mantle, shown in blue for SLB11 and red for SLB21. Panels (c1–c3) and (d1–d3) show the resulting mineralogical phase diagrams based on the SLB11 and SLB21 models. Each color represents a specific mineral, as indicated in the legend. The black line indicates the temperature profile used to compute both the mineralogical phase proportions and the seismic velocity profiles shown in (a) and (b). For a given mantle composition, the temperature profile shown in (c) and (d) are similar. Rectangles in panels (c1) and (d1–d3) highlight zoomed-in regions of particular interest within the phase diagrams. The Mg# considered are 0.739, 0.767, and 0.766 for EH45, TA, and YM, respectively.

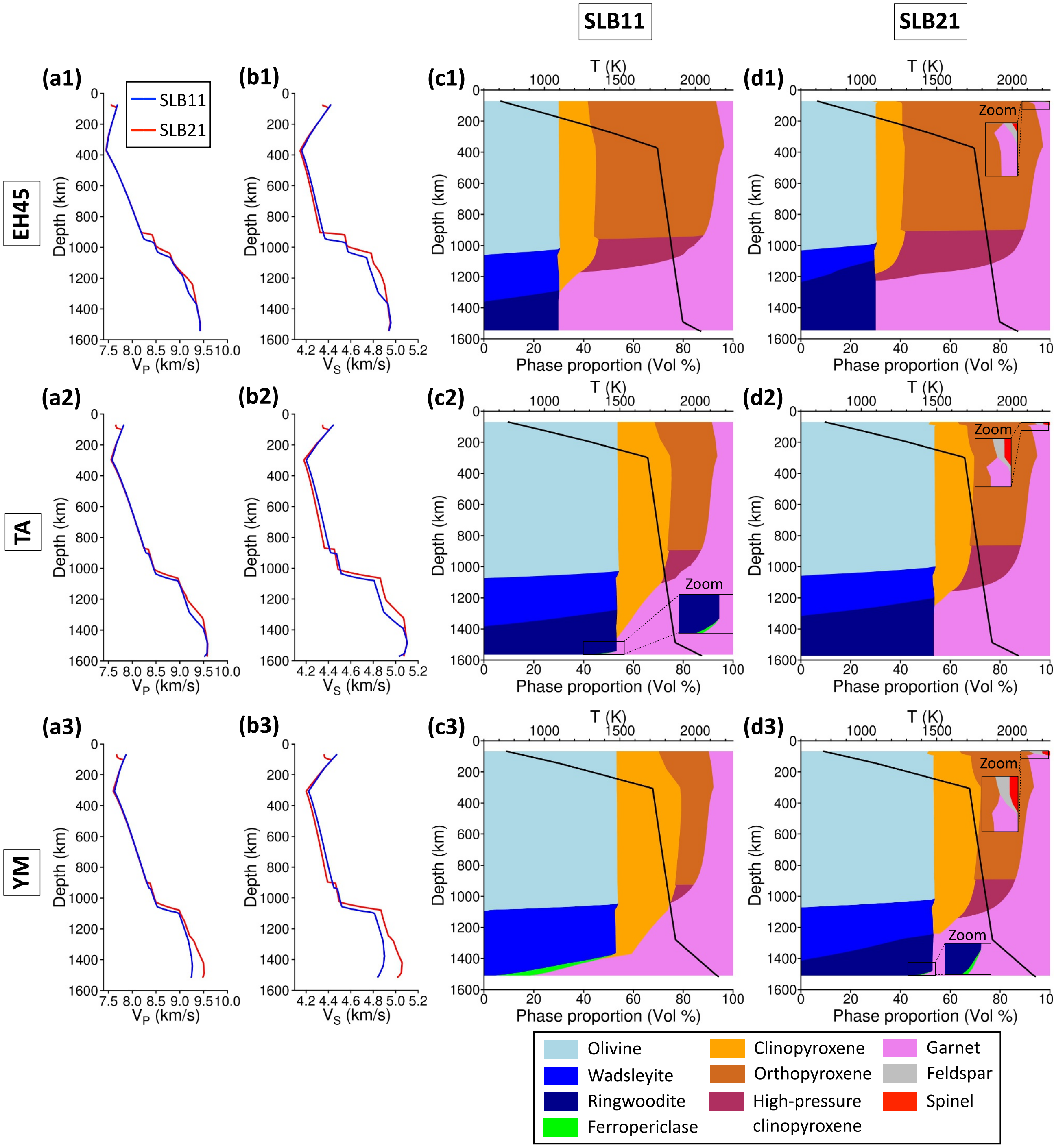

Figure 12. Comparison of seismic velocities and mineralogical phase diagrams between SLB11 and SLB21 for BML models, using a given temperature profile and Mg#. The three rows present results for the EH45, TA, and YM mantle compositions. Panels (a1–a3) and (b1–b3) display the output V_P and V_S profiles in the mantle, shown in blue for SLB11 and red for SLB21. Panels (c1–c3) and (d1–d3) show the resulting mineralogical phase diagrams based on the SLB11 and SLB21 models. Each color represents a specific mineral, as indicated in the legend. The black line indicates the temperature profile used to compute both the mineralogical phase proportions and the seismic velocity profiles shown in (a) and (b). For a given mantle composition, the temperature profile shown in (c) and (d) are similar. Rectangles in panels (c1) and (d1–d3) highlight zoomed-in regions of particular interest within the phase diagrams. The Mg# considered are 0.738, 0.756, and 0.761 for EH45, TA, and YM, respectively.

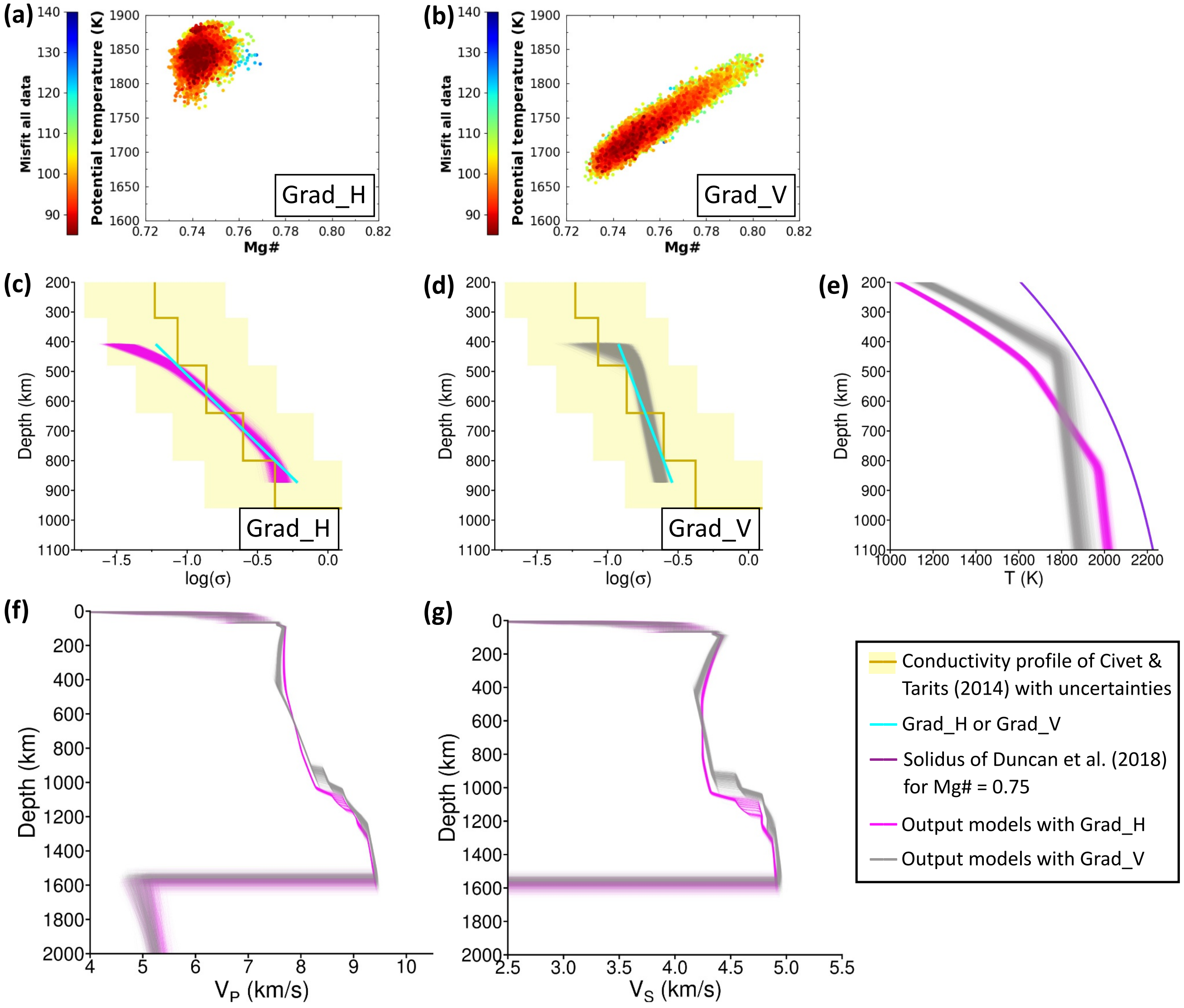

Figure 13. Inversion results using two different input electrical conductivity profiles (Grad_H and Grad_V) for non-BML models, considering the EH45 mantle composition. Panels (a, b) show the potential temperature (T_p) as a function of Mg#, along with the data misfit estimates for Grad_H and Grad_V, respectively. Red and blue colors are small and large misfit values, respectively. Panels (c, d) display the input electrical conductivity profiles (Grad_H and Grad_V), shown in cyan, which are used as input data in the inversion. The corresponding output conductivity profiles are shown in magenta (c) and gray (d). The conductivity profile from Civet and Tarits (2014) is shown in khaki, with its uncertainty range represented in yellow. Panels (e–g) present the output temperature, V_P, and V_S profiles, in magenta for Grad_H and in gray for Grad_V.

Currently, the geophysical data sets that we use are not sufficiently sensitive to be affected by the sharpness of seismic discontinuities, making it impossible to determine which of the two thermodynamic databases provides a better fit to the observations (Figures S6.1 and S6.2 in Supporting Information S1). InSight receiver function analyzes (e.g., Knapmeyer-Endrun et al., 2021) have not probed seismic discontinuities deeper than the Moho, and these measurements reflect only the crustal structure beneath the InSight lander. It is therefore remains unclear whether the discontinuity observed at approximately 80 km depth, associated with the transformation of feldspar and spinel into garnet, actually exists. In addition, the available constraints on the deep mantle are extremely limited: the electrical conductivity profile of Civet and Tarits (2014) is highly uncertain below 900 km depth, and only two seismic events capable of sampling the deep mantle have been recorded (S0976a and S1000a). These data alone are insufficient at that time to constrain the complexity of the upper and deep mantle mineralogy.

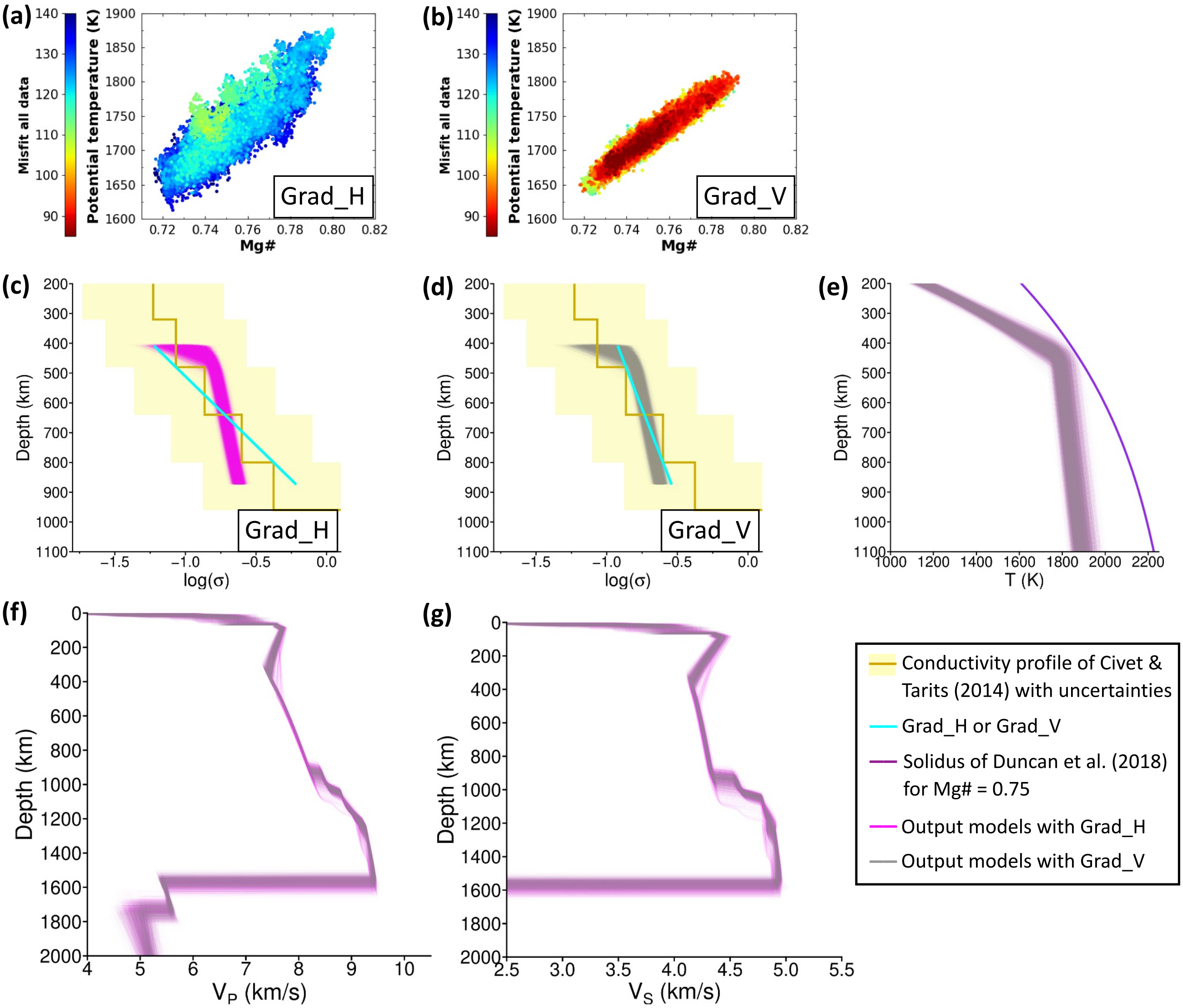

Figure 14. Inversion results using two different input electrical conductivity profiles (Grad_H and Grad_V) for BML models, considering the EH45 mantle composition. Panels (a, b) show the potential temperature (T_p) as a function of Mg#, along with the data misfit estimates for Grad_H and Grad_V, respectively. Red and blue colors are small and large misfit values, respectively. Panels (c, d) display the input electrical conductivity profiles (Grad_H and Grad_V), shown in cyan, which are used as input data in the inversion. The corresponding output conductivity profiles are shown in magenta (c) and gray (d). The conductivity profile from Civet and Tarits (2014) is shown in khaki, with its uncertainty range represented in yellow. Panels (e–g) present the output temperature, V_P, and V_S profiles, in magenta for Grad_H and in gray for Grad_V.

5.2. Influence of Conductivity Profile Uncertainties

As explained in Section 2, to overcome the layer-based parameterization of the Civet and Tarits (2014) profile, we consider a smoothed version of it. However, due to the relatively large uncertainties associated with this profile (0.5 log units), we cannot rule out the possibility that its slope differs somewhat from the one used as input in our inversions. To better assess how uncertainties in the slope of the electrical conductivity profile estimated by Civet and Tarits (2014) affect our results, we tested the effect of two alternative slope values.

Considering the EH45 mantle composition, we re-ran our inversion algorithm using two modified electrical conductivity profile with different gradients as input: one shallower (referred to as Grad_H) and one steeper (Grad_V), compared to the profile used in Section 4, as shown in Figures 13c, 13d, 14c, and 14d. The results show that non-BML models can reproduce both Grad_H and Grad_V equally well, with similar misfit values (Figures 13a and 13b). The models retrieved for Grad_H closely resemble the F1 models described in Section 4, characterized by thicker lithospheric and upper thermal boundary layers (D_{lu}), whereas those obtained for Grad_V are very similar to the F2 models, which exhibit smaller D_{lu}. For BML models (Figure 14), Grad_V is well reproduced and yields results very similar to those presented in Section 4. In contrast, the predicted electrical conductivity profiles of BML models deviate significantly from Grad_H: the resulting conductivity profiles remain steep, as D_{lu} cannot reach the larger values observed in non-BML models, resulting in larger misfit values (Figures 14a and 14b). This is in part due to the thinner lithosphere inferred for models that include a BML (see Section 4.4).

These results highlight the importance of conducting new ground-based geophysical investigations involving electromagnetic soundings, as pointed out in Ruedas and Breuer (2021). More accurate estimates of the electrical conductivity in the Martian mantle, with uncertainties at least twice as small as those reported by Civet and Tarits (2014), would substantially restrict the range of consistent models.

6. Conclusions

In the context of planetary exploration, geophysical data remain sparse and generally have larger uncertainties than their terrestrial counterparts. In this study, we proposed a synergetic strategy that simultaneously inverts multiple types of geophysical observations using a probabilistic framework to constrain the one-dimensional structure of Mars. By formally linking thermal and compositional parameters through a self-consistent thermochemical evolution model (e.g., Drilleau et al., 2021; Samuel et al., 2019), our approach enables the joint inference of the present-day interior structure and its long-term dynamic evolution. The method also incorporates information derived from laboratory experiments in mineral physics and petrology (Stixrude & Lithgow-Bertelloni, 2021). Compared to our previous studies (e.g., Drilleau et al., 2022, 2024; Irving et al., 2023; Samuel et al., 2023; Stähler et al., 2021), we incorporated the electrical conductivity data from Civet and Tarits (2014), which has different sensitivities to temperature and composition than seismic data and k_2. In addition, the Mg# is a model parameter in our setting and inferred from the data. We systematically tested how three different mantle compositions (EH45, TA, and YM) for both non-BML and BML models affected our results. Finally, we relied on an updated thermodynamic database from Stixrude and Lithgow-Bertelloni (2021) compared to the previous database from Stixrude and Lithgow-Bertelloni (2011).

Our findings demonstrate that combining seismic, geodetic, and electrical conductivity data within a joint inversion framework substantially reduces the range of admissible interior structure models. One of the key conclusions is that BML models provide a poorer fit to the electrical conductivity data, even though this result must be interpreted with caution due to the significant uncertainties in the Civet and Tarits (2014)'s profile. For non-BML models, the joint inversion results reveal that two families of models are capable of fitting the three data sets. Although their relative prevalence varies depending on the assumed mantle composition, both families share the same characteristics: Family F1 is defined by a smaller Mg# and a larger T_p, while Family F2 is characterized by a larger Mg# and a smaller T_p. Although both families produce comparable fits to the differential body wave arrival times and k_2, they differ in their ability to reproduce the electrical conductivity profile of Civet and Tarits (2014). Due to their thicker lithospheric and upper thermal boundary layer D_{l_u}, F1 models provide a better fit to the observed conductivity profile. For BML models, only models with a thin D_{l_u} exist, and those based on the YM composition exhibit a significantly poorer fit to the seismic data when all three data sets are jointly inverted. In contrast, models based on EH45 and TA yield fits to the seismic data and k_2 that are comparable to those of the non-BML models, with the additional advantage of better reproducing the diffracted P-wave arrival time recorded during sol 1,000 of the InSight mission. However, the predicted electrical conductivity profiles reproduce the slope of the Civet and Tarits (2014)'s conductivity profile less accurately than non-BML models. This discrepancy is mainly due to the thinner lithosphere inferred for BML models.

To further constrain models of Mars' interior structure, it is essential to extract more information from the seismic record, particularly regarding reflected and refracted seismic phases along seismic discontinuities associated with mineralogical phase transitions occurring in the Martian mantle. Based on the only published seismic estimates of the depth of the olivine to wadsleyite transition (Huang et al., 2022), only non-BML models with the EH45 composition are consistent with the depth range proposed by Huang et al. (2022). In contrast, the vast majority of BML models, regardless of the assumed mantle composition, reproduce this seismic discontinuity at the depth reported in Huang et al. (2022). However, in our current study, we also showed that the depth and nature of these mineralogical phase transitions are highly sensitive to the thermodynamic database used. The mantle solidus can also plays an important role in determining the acceptability of models, particularly for BML models, whose temperature values at the top of the convecting mantle are very close to the solidus. Another important point concerns the 180 km layer-based parameterization of the electrical conductivity profile from Civet and Tarits (2014), which is associated with relatively large uncertainties. In this study, we showed that ambiguity in interpreting the slope of this profile can significantly influence model selection, shifting preference between the F1 and F2 families for non-BML models, or between BML and non-BML models. Additional constraints from electromagnetic data sensitive to the crust, such as the C-responses (the ratio of the vertical magnetic field component to the spatial derivative of the horizontal components) recently derived from InSight data by Mittleholz et al. (2025), could further help discriminate between competing interior models. While the InSight mission has considerably improved our understanding of Mars' deep interior, additional seismic and electromagnetic investigations are required to refine our knowledge about the deep interior.

Conflict of Interest

The authors declare no conflicts of interest relevant to this study.

Data Availability Statement

All raw waveform seismic data is available through IPGP data center (InSight Mars SEIS Data Service, 2019a), IRIS-DMC (InSight Marsquake Service, 2023), and NASA-PDS (InSight Mars SEIS Data Service, 2019b). Body wave arrival times are provided in Drilleau et al. (2024) and Samuel et al. (2023). The electrical conductivity profile is provided in Civet and Tarits (2014). All the computations made in this article are based on codes described in published papers that are cited in the reference list. The Monte Carlo inversion code is described in Drilleau et al. (2021). The travel time code `TauP` is described in Crotwell et al. (1999) and is available at https://www.seis.sc.edu/taup/. The `Perple_X` Gibbs free energy minimization code is described in Connolly (2009) and is available at https://www.perplex.ethz.ch. The figures were created with Matplotlib (Hunter, 2007) and The Generic Mapping Tools (Wessel et al., 2019).

Acknowledgments

We would like to thank Anastassia Borisova, Julien Berger, and Bob Myhill for fruitful discussions. We also thank François Civet and Pascal Tarits for providing us with electrical conductivity profile derived from MGS measurements. We also thank James A. D. Connolly for answering our questions regarding Perple_X. The authors acknowledge two anonymous reviewers for their constructive comments that helped to improve this paper. M.D. was granted access to the GENCI HPC resources of IDRIS under allocation AD010413017R3. Numerical computations were partly performed on the S-CAPAD/DANTE platform, IPGP, France. M.D., H.S., R.F. G., and P.L. thank CNES (French Space Agency) for funding this study through SEIS/InSight APR projects. A.R. was financially supported by the Belgian PRODEX program by the European Space Agency in collaboration with the Belgian Federal Science Policy Office, contract number PEA4000140326.

References

Afonso, J., Fullea, J., Yang, Y., Connolly, J., & Jones, A. (2013). 3-D multi-observable probabilistic inversion for the compositional and thermal structure of the lithosphere and upper mantle. II: General methodology and resolution analysis. *Journal of Geophysical Research: Solid Earth*, *118*(4), 1650–1676. https://doi.org/10.1002/jgrb.50123

Alterman, Z., Jarosh, H., & Perekis, C. L. (1959). Oscillations of the Earth. *Proceedings of the Royal Society A: Mathematical, Physical and Engineering Sciences*, *252*(1268), 80–95.

Banerdt, W. B., Smrekar, S. E., Banfield, D., Giardini, D., Golombek, M., Johnson, C. L., et al. (2020). Initial results from the InSight mission on Mars. *Nature Geoscience*, *13*(3), 1–14. https://doi.org/10.1038/s41561-020-0544-y

Civet, F., & Tarits, P. (2014). Electrical conductivity of the mantle of Mars from MGS magnetic observations. *Earth Planets and Space*, *66*(1), 85. https://doi.org/10.1186/1880-5981-66-85

Collinet, M., Médard, E., Charlier, B., Auwera, J. V., & Grove, T. L. (2015). Melting of the primitive Martian mantle at 0.5–2.2 GPa and the origin of basalts and alkaline rocks on Mars. *Earth and Planetary Science Letters*, *427*, 83–94. https://doi.org/10.1016/j.epsl.2015.06.056

Collinet, M., Plesa, A.-C., Ruedas, T., Schwinger, S., & Breuer, D. (2023). The temperature and composition of the mantle sources of Martian basalts. *Geophysical Research Letters*, *50*(11), e2023GL103537. https://doi.org/10.1029/2023GL103537

Connolly, J. A. D. (2005). Computation of phase equilibria by linear programming: A tool for geodynamic modeling and its application to subduction zone decarbonation. *Earth and Planetary Science Letters*, *236*(1–2), 524–541. https://doi.org/10.1016/j.epsl.2005.04.033

Connolly, J. A. D. (2009). The geodynamic equation of state: What and how. *Geochemistry, Geophysics, Geosystems*, *10*(10). https://doi.org/10.1029/2009GC002540

Crotwell, H. P., Owens, T. J., & Ritsema, J. (1999). The TauP Toolkit: Flexible seismic travel-time and ray-path utilities. *Seismological Research Letters*, *70*(2), 154–160. https://doi.org/10.1785/gssrl.70.2.154

Drilleau, M., Samuel, H., Garcia, R. F., Rivoldini, A., Perrin, C., Michaut, C., et al. (2022). Marsquake locations and 1-D seismic models for Mars from InSight data. *Journal of Geophysical Research: Planets*, *127*(9), e2021JE007067. https://doi.org/10.1029/2021JE007067

Drilleau, M., Samuel, H., Garcia, R. F., Rivoldini, A., Perrin, C., Wieczorek, M., et al. (2024). Constraints on lateral variations of Martian crustal thickness from seismological and gravity field measurements. *Geophysical Research Letters*, *51*(4), e2023GL105701. https://doi.org/10.1029/2023GL105701

Drilleau, M., Samuel, H., Rivoldini, A., Panning, M., & Lognonné, P. (2021). Bayesian inversion of the Martian structure using geodynamic constraints. *Geophysical Journal International*, *226*(3), 1615–1644. https://doi.org/10.1093/gji/ggab105

Duncan, M. S., Schmerr, N. C., Bertka, C. M., & Fei, Y. (2018). Extending the solidus for a model iron-rich Martian mantle composition to 25 GPa. *Geophysical Research Letters*, *45*(19), 10211–10220. https://doi.org/10.1029/2018GL078182

Durán, C., Khan, A., Ceylan, S., Zenhäusern, G., Stähler, S., Clinton, J., & Giardini, D. (2022). Seismology on Mars: An analysis of direct, reflected, and converted seismic body waves with implications for interior structure. *Physics of the Earth and Planetary Interiors*, 106851. https://doi.org/10.1016/j.pepi.2022.106851

Elkins-Tanton, L. (2008). Linked magma ocean solidification and atmospheric growth for Earth and Mars. *Earth and Planetary Science Letters*, *271*(1), 181–191. https://doi.org/10.1016/j.epsl.2008.03.062

Fullea, J. (2017). On joint modelling of electrical conductivity and other geophysical and petrological observables to infer the structure of the lithosphere and underlying upper mantle. *Surveys in Geophysics*, *38*(5), 963–1004. https://doi.org/10.1007/s10712-017-9432-4

Grayver, A. (2024). Unravelling the electrical conductivity of Earth and planets. *Surveys in Geophysics*, *45*(1), 187–238. https://doi.org/10.1007/s10712-023-09813-9

Grimm, R. E., Mittelholz, A., & Johnson, C. L. (2024). Geomagnetic depth sounding of the Martian mantle from InSight. In *55th lunar and planetary science conference* (Vol. 3040, p. 2569).

Guerrero, J. M., Deschamps, F., Li, Y., Hsieh, W. P., & Tackley, P. J. (2023). Influence of heterogeneous thermal conductivity on the long-term evolution of the lower-mantle thermochemical structure: Implications for primordial reservoirs. *Solid Earth*, *14*(2), 119–135. https://doi.org/10.5194/se-14-119-2023

Han, K., & Clark, S. M. (2021). Review of calculating the electrical conductivity of mineral aggregates from constituent conductivities. *Solid Earth Sciences*, *6*(2), 111–128. https://doi.org/10.1016/j.sesci.2021.02.003

Horleston, A. C., Clinton, J. F., Ceylan, S., Giardini, D., Charalambous, C., Irving, J. C. E., et al. (2022). The far side of Mars: Two distant marsquakes detected by InSight. *The Seismic Record*, *2*(2), 88–99. https://doi.org/10.1785/0320220007

Hsieh, W. P., Chang, Y. Y., Tsao, Y. C., Lin, C. H., & Vilella, K. (2024). Exceptionally low thermal conduction of basaltic glasses and implications for the thermo-chemical evolution of the Earth's primitive magma ocean. *Journal of Geophysical Research: Solid Earth*, *129*(2), 1–10. https://doi.org/10.1029/2023JB027722

Hsieh, W. P., Deschamps, F., Okuchi, T., & Lin, J. F. (2018). Effects of iron on the lattice thermal conductivity of Earth's deep mantle and implications for mantle dynamics. *Proceedings of the National Academy of Sciences of the United States of America*, *115*(16), 4099–4104. https://doi.org/10.1073/pnas.1718557115

Huang, Q., Schmerr, N. C., King, S. D., Kim, D., Rivoldini, A., Plesa, A.-C., et al. (2022). Seismic detection of a deep mantle discontinuity within Mars by InSight. *Proceedings of the National Academy of Sciences*, *119*(42), e2204474119. https://doi.org/10.1073/pnas.2204474119

Hunter, J. D. (2007). Matplotlib: A 2D graphics environment. *Computing in Science & Engineering*, *9*(3), 90–95. https://doi.org/10.1109/MCSE.2007.55

InSight Mars SEIS Data Service. (2019a). Seis raw data, InSight mission [Dataset]. *IPGP, JPL, CNES, ETHZ, ICL, MPS, ISAE-Supaero, LPG, MFSC*. https://doi.org/10.18715/SEIS.INSIGHT.XB_2016

InSight Marsquake Service. (2023). Mars seismic catalogue, InSight mission; v13 2023-01-01 [Dataset]. *ETHZ, IPGP, JPL, ICL, Univ. Bristol*. https://doi.org/10.12686/a19

InSight Mars SEIS Data Service. (2019b). InSight SEIS data bundle [Dataset]. *PDS Geosciences (GEO) node*. https://doi.org/10.17189/1517570

Irving, J. C. E., Cottaar, S., & Lekić, V. (2018). Seismically determined elastic parameters for Earth's outer core. *Science Advances*, *4*(6), eaar2538. https://doi.org/10.1126/sciadv.aar2538

Irving, J. C. E., Lekić, V., Duran, C., Drilleau, M., Kim, D., Rivoldini, A., et al. (2023). First observations of core-transiting seismic phases on Mars. *Proceedings of the National Academy of Sciences*, *120*(18), e2217090120. https://doi.org/10.1073/pnas.2217090120

Katsura, T., Yokoshi, S., Kawabe, K., Shatskiy, A., Okube, M., Fukui, H., et al. (2007). Pressure dependence of electrical conductivity of (Mg,Fe)SiO_3 ilmenite. *Physics and Chemistry of Minerals*, *34*(4), 249–255. https://doi.org/10.1007/s00269-007-0143-0

Khan, A. (2016). On Earth's mantle constitution and structure from joint analysis of geophysical and laboratory-based data: An example. *Surveys in Geophysics*, *37*(1), 149–189. https://doi.org/10.1007/s10712-015-9353-z

Khan, A., Ceylan, S., van Driel, M., Giardini, D., Lognonné, P., Samuel, H., et al. (2021). Upper mantle structure of Mars from InSight seismic data. *Science*, *373*(6553), 434–438. https://doi.org/10.1126/science.abf2966

Khan, A., & Connolly, J. A. D. (2008). Constraining the composition and thermal state of Mars from inversion of geophysical data. *Journal of Geophysical Research*, *113*(E7). https://doi.org/10.1029/2007JE002996

Khan, A., Liebske, C., Rozel, A., Rivoldini, A., Nimmo, F., Connolly, J. A. D., et al. (2018). A geophysical perspective on the bulk composition of Mars. *Journal of Geophysical Research: Planets*, *224*(2–4), 575–611. https://doi.org/10.1002/2017JE005371

Knapmeyer-Endrun, B., Panning, M. P., Bissig, F., Joshi, R., Khan, A., Kim, D., et al. (2021). Thickness and structure of the Martian crust from InSight seismic data. *Science*, *373*(6553), 438–443. https://doi.org/10.1126/science.abf8966

Konopliv, A. S., Park, R. S., Rivoldini, A., Baland, R. M., Le Maistre, S., Van Hoolst, T., et al. (2020). Detection of the Chandler wobble of Mars from orbiting spacecraft. *Geophysical Research Letters*, *47*(21), 1–9. https://doi.org/10.1029/2020GL090568

Le Maistre, S., Rivoldini, A., Caldiero, A., Yseboodt, M., Baland, R.-M., Beuthe, M., et al. (2023). Spin state and deep interior structure of Mars from InSight radio tracking. *Nature*, *619*(7971), 733–737. https://doi.org/10.1038/s41586-023-06150-0

Li, J., Hua, J., Ferrand, T. P., Pou, L., Huang, Q., Allibert, L., et al. (2025). Evidence for weak seismic attenuation in Mars' deep mantle. *Communications Earth & Environment*, *6*(1), 1–11. https://doi.org/10.1038/s43247-025-02664-9

Lognonne, P., Banerdt, W. B., Giardini, D., Pike, W. T., Christensen, U., Laudet, P., et al. (2019). SEIS: InSight' seismic experiment for internal structure of Mars. *Space Science Reviews*, *215*(1), 12. https://doi.org/10.1007/s11214-018-0574-6

Metropolis, N., Rosenbluth, A. W., Rosenbluth, M. N., Teller, A. H., & Teller, E. (1953). Equation of state calculations by fast computing machines. *Journal of Chemical Physics*, *21*(6), 1087–1091. https://doi.org/10.1063/1.1699114

Mittleholz, A., Grayver, A., Johnson, C. L., & Munch, F. (2025). Electromagnetic sounding of Mars with InSight. In *56th lunar and planetary science conference* (p. 1979).

Mittleholz, A., Grimm, R., Johnson, C. L., Langlais, B., Khan, A., Verhoeven, O., et al. (2020). Towards magnetic sounding of the Martian mantle. In *51th lunar and planetary science conference* (p. 2157).

Mocquet, A., & Menvielle, M. (2000). Complementarity of seismological and electromagnetic sounding methods for constraining the structure of the Martian mantle. *Planetary and Space Science*, *48*(12), 1249–1260. https://doi.org/10.1016/S0032-0633(00)00107-0

Naif, S., Selway, K., Murphy, B. S., Egbert, G., & Pommier, A. (2021). Electrical conductivity of the lithosphere-asthenosphere system. *Physics of the Earth and Planetary Interiors*, *313*, 106661. https://doi.org/10.1016/j.pepi.2021.106661

Posiolova, L. V., Lognonné, P., Banerdt, W. B., Clinton, J., Collins, G. S., Kawamura, T., et al. (2022). Largest recent impact craters on Mars: Orbital imaging and surface seismic co-investigation. *Science*, *378*(6618), 412–417. https://doi.org/10.1126/science.abq7704

Pou, L., Nimmo, F., Rivoldini, A., Khan, A., Bagheri, A., Gray, T., et al. (2022). Tidal constraints on the Martian interior. *Journal of Geophysical Research: Planets*, *127*(11), e2022JE007291. https://doi.org/10.1029/2022JE007291

Ruedas, T., & Breuer, D. (2021). Electrical and seismological structure of the Martian mantle and the detectability of impact-generated anomalies. *Icarus*, *358*, 114176. https://doi.org/10.1016/j.icarus.2020.114176

Samuel, H., Ballmer, M. D., Padovan, S., Tosi, N., Rivoldini, A., & Plesa, A.-C. (2021). The thermo-chemical evolution of Mars with a strongly stratified mantle. *Journal of Geophysical Research: Planets*, *126*(4), e2020JE006613. https://doi.org/10.1029/2020JE006613

Samuel, H., Drilleau, M., Rivoldini, A., Xu, Z., Huang, Q., Garcia, R. F., et al. (2023). Geophysical evidence for an enriched molten silicate layer above Mars's core. *Nature*, *622*(7984), 712–717. https://doi.org/10.1038/s41586-023-06601-8

Samuel, H., Lognonné, P. H., Panning, M., & Lainey, V. (2019). The rheology and thermal history of Mars revealed by the orbital evolution of Phobos. *Nature*, *569*(7757), 523–527. https://doi.org/10.1038/s41586-019-1202-7

Sanloup, C., Jambon, A., & Gillet, P. (1999). A simple chondritic model of Mars. *Physics of the Earth and Planetary Interiors*, *112*(1–2), 43–54. https://doi.org/10.1016/s0031-9201(98)00175-7

Stähler, S. C., Khan, A., Banerdt, W. B., Lognonné, P., Giardini, D., Ceylan, S., et al. (2021). Seismic detection of the Martian core. *Science*, *373*(6553), 443–448. https://doi.org/10.1126/science.abi7730

Stixrude, L., & Lithgow-Bertelloni, C. (2011). Thermodynamics of mantle minerals—II. Phase equilibria. *Geophysical Journal International*, *184*(3), 1180–1213. https://doi.org/10.1111/j.1365-246X.2010.04890.x

Stixrude, L., & Lithgow-Bertelloni, C. (2021). Thermal expansivity, heat capacity and bulk modulus of the mantle. *Geophysical Journal International*, *228*(2), 1119–1149. https://doi.org/10.1093/gji/ggab394

Takeuchi, H., & Saito, M. (1972). Seismic surfaces waves. In B. A. Bolt (Ed.), *Methods in computational physics* (Vol. 1, pp. 217–294). Academic Press.

Tarantola, A. (2005). *Inverse problem theory—And methods for model parameter estimation*. SIAM.

Taylor, G. J. (2013). The bulk composition of Mars. *Chemie der Erde*, *73*(4), 401–420. https://doi.org/10.1016/j.chemer.2013.09.006

Vacher, P., & Verhoeven, O. (2007). Modelling the electrical conductivity of iron-rich minerals for planetary applications. *Planetary and Space Science*, *55*(4), 455–466. https://doi.org/10.1016/j.pss.2006.10.003

Verhoeven, O., Mocquet, A., Vacher, P., Rivoldini, A., Menvielle, M., Arrial, P.-A., et al. (2009). Constraints on thermal state and composition of the Earth's lower mantle from electromagnetic impedances and seismic data. *Journal of Geophysical Research*, *114*(B3). https://doi.org/10.1029/2008JB005678

Verhoeven, O., Rivoldini, A., Vacher, P., Mocquet, A., Choblet, G., Menvielle, M., et al. (2005). Interior structure of terrestrial planets: Modeling Mars' mantle and its electromagnetic, geodetic, and seismic properties. *Journal of Geophysical Research*, *110*(E4). https://doi.org/10.1029/2004JE002271

Verhoeven, O., & Vacher, P. (2016). Laboratory-based electrical conductivity at Martian mantle conditions. *Planetary and Space Science*, *134*, 29–35. https://doi.org/10.1016/j.pss.2016.10.005

Wang, Q., Bagdassarov, N., Xia, Q.-K., & Zhu, B. (2014). Water contents and electrical conductivity of peridotite xenoliths from the north China Craton: Implications for water distribution in the upper mantle. *Lithos*, *189*, 105–126. https://doi.org/10.1016/j.lithos.2013.08.005

Wänke, H., Dreibus, G., & Wright, I. P. (1994). Chemistry and accretion history of Mars. *Philosophical Transactions of the Royal Society of London,Series A: Physical and Engineering Sciences*, *349*(1690), 285–293. https://doi.org/10.1098/rsta.1994.0132

Wasson, J. T., & Kallemeyn, G. W. (1988). Compositions of chondrites. *Philosophical Transactions of the Royal Society of London A: Mathematical, Physical and Engineering Sciences*, *325*(1587), 535–544. https://doi.org/10.1098/rsta.1988.0066

Wessel, P., Luis, J. F., Uieda, L., Scharroo, R., Wobbe, F., Smith, W. H. F., & Tian, D. (2019). The generic mapping tools version 6. *Geochemistry, Geophysics, Geosystems*, *20*(11), 5556–5564. https://doi.org/10.1029/2019GC008515

Wieczorek, M. A., Broquet, A., McLennan, S. M., Rivoldini, A., Golombek, M., Antonangeli, D., et al. (2022). InSight constraints on the global character of the Martian crust. *Journal of Geophysical Research: Planets*, *127*(5), e2022JE007298. https://doi.org/10.1029/2022JE007298

Wieczorek, M. A., & Zuber, M. T. (2004). Thickness of the Martian crust: Improved constraints from geoid-to-topography ratios. *Journal of Geophysical Research*, *109*(E1). https://doi.org/10.1029/2003JE002153

Xu, Y., Shankland, T., & Duba, A. (2000). Pressure effect on electrical conductivity of mantle olivine. *Physics of the Earth and Planetary Interiors*, *118*(1), 149–161. https://doi.org/10.1016/S0031-9201(99)00135-1

Yang, X., Keppler, H., McCammon, C., & Ni, H. (2012). Electrical conductivity of orthopyroxene and plagioclase in the lower crust. *Contributions to Mineralogy and Petrology*, *163*(1), 33–48. https://doi.org/10.1007/s00410-011-0657-9

Yoder, C. F., Konopliv, A. S., Yuan, D. N., Standish, E. M., & Folkner, W. M. (2003). Fluid core size of Mars from detection of the solar tide. *Science*, *300*(5617), 299–303. https://doi.org/10.1126/science.1079645

Yoshino, T. (2010). Laboratory electrical conductivity measurement of mantle minerals. *Surveys in Geophysics*, *31*(2), 163–206. https://doi.org/10.1007/s10712-009-9084-0

Yoshino, T., Shimojuku, A., & Li, D. (2014). Electrical conductivity of stishovite as a function of water content. *Physics of the Earth and Planetary Interiors*, *227*, 48–54. https://doi.org/10.1016/j.pepi.2013.12.003

Yoshizaki, T., & McDonough, W. F. (2020). The composition of Mars. *Geochimica et Cosmochimica Acta*, *273*, 137–162. https://doi.org/10.1016/j.gca.2020.01.011

References From the Supporting Information

Bills, B. G., Neumann, G. A., Smith, D. E., & Zuber, M. T. (2005). Improved estimate of tidal dissipation within Mars from MOLA observations of the shadow of Phobos. *Journal of Geophysical Research*, *110*(E7). https://doi.org/10.1029/2004JE002376

Efroimsky, M., & Lainey, V. (2007). Physics of bodily tides in terrestrial planets and the appropriate scales of dynamical evolution. *Journal of Geophysical Research*, *112*(E12), E07004. https://doi.org/10.1029/2007JE002908

Guinard, A., Fienga, A., Mémim, A., & Ganino, C. (2025). Coupled tidal tomography and thermal constraints for probing Mars viscosity profile. *Icarus*, *425*, 116318. https://doi.org/10.1016/j.icarus.2024.116318

Jackson, I., & Faul, U. H. (2010). Grainsize-sensitive viscoelastic relaxation in olivine: Towards a robust laboratory-based model for seismological application. *Physics of the Earth and Planetary Interiors*, *183*(1–2), 151–163. https://doi.org/10.1016/j.pepi.2010.09.005

Jackson, I., Fitz Gerald, J. D., Faul, U. H., & Tan, B. H. (2002). Grain-size-sensitive seismic wave attenuation in polycrystalline olivine. *Journal of Geophysical Research*, *107*(B12), 1–16. https://doi.org/10.1029/2001JB001225

Khan, A., Mosegaard, K., Williams, J. G., & Lognonné, P. (2004). Does the Moon possess a molten core? Probing the deep lunar interior using results from LLR and Lunar Prospector. *Journal of Geophysical Research*, *109*(9), 80. https://doi.org/10.1029/2004JE002294

Kim, D., Banerdt, W. B., Ceylan, S., Giardini, D., Lekić, V., Lognonné, P., et al. (2022). Surface waves and crustal structure on Mars. *Science*, *378*(6618), 417–421. https://doi.org/10.1126/science.abq7157

Renaud, J. P., & Henning, W. G. (2018). Increased tidal dissipation using realistic rheological models: Implications for the thermal history of Io and tidally active extrasolar planets. *The Astrophysical Journal*, *857*(2), 1–30.

Smrekar, S. E., Lognonné, P., Spohn, T., Banerdt, B., Breuer, D., Christensen, U., et al. (2019). Pre-mission InSights on the interior of Mars. *Space Science Reviews*, *215*(1), 3. https://doi.org/10.1007/s11214-018-0563-9